Nonlinear Dyn
https://doi.org/10.1007/s11071-024-10621-y

RESEARCH

Mem-modeling of strain ratcheting using early-time soil fatigue data

Jin-Song Pei · Joseph P. Wright · Gerald A. Miller · François Gay-Balmaz · Marco B. Quadrelli

Received: 5 September 2024 / Accepted: 6 November 2024

Abstract Stress–strain behavior of two different soil specimens subjected to cyclic compressive loading are studied herein, the goal being to present a simple dynamic uniaxial mem-modeling approach that aids physical insight and enables system identification. In this paper, "mem" stands for memory, i.e., hysteresis. Mem-models are hysteresis models transferred from electrical engineering using physical analogies. Connected in series, a mem-dashpot and mem-spring are employed to model inter-cycle strain ratcheting and intra-cycle gradual densification of the two soil specimens. Measured time histories of stress and strain are first decomposed so that the two modeling components, mem-dashpot and mem-spring, can be identified separately. This paper focuses on the mem-dashpot, a nonlinear generalization of a linear viscous damper. A mem-spring model is also devised built on an extended Masing model. Nonlinear dynamic simulations (with inertia) employing the identified mem-dashpot and mem-spring demonstrate how well the identified mem-models reproduce the measured early-time data (first 200 cycles of loading). Choices of state variables inherited from bond graph theory, the root of mem-models, are introduced, while MATLAB time integrators (i.e., ode solvers) are used throughout this study to explore a range of contrasting damper and spring models. Stiff solver and the state event location algorithm are employed to solve the equations of motion involving piecewise-defined restoring forces (when applicable). Computational details and results are relegated to the appendices. This is the first study to use single-degree-of-freedom (SDOF) system dynamic simulations to explore the consistency of mem-models identified from real-world data.

Keywords Soil dynamics · Compressive loading · Strain ratcheting · Cyclic triaxial tests · Time-varying system · Hysteresis · Mem-models · Generalized momentum · Absement · Parametric plot · SDOF dynamic simulation · Choice of state variables · State event location algorithm · ode45 · ode15s · Stiff solver

J.-S. Pei (✉) · G. A. Miller
School of Civil Engineering and Environmental Science, University of Oklahoma, Norman, Oklahoma 73019, USA
e-mail: jspei@ou.edu

J. P. Wright
Weidlinger Applied Science, New York, NY 10005, USA

F. Gay-Balmaz
School of Physical and Mathematical Sciences, Nanyang Technological University, Singapore 639798, Singapore

M. B. Quadrelli
Robotics Modeling and Simulation Group, Jet Propulsion Laboratory, California Institute of Technology, Pasadena, CA 91109, USA

1 Introduction

Many problems facing geotechnical engineers require understanding of, and the ability to model the dynamic behavior of geomaterials. Examples include highway and railway substructures, and other dynamically loaded foundation systems. It is important to quantify material damage associated with repeated dynamic loading to assess the useful life of these systems. This is particularly important in light of the additional stressors from climate change and increased frequency of natural hazards. The finite element method (FEM) and discrete element method (DEM) are two ways to simulate and predict potential damage by using assumed boundary conditions, loading conditions and constitutive relations, where measured data are utilized in an indirect manner; this is called forward analysis. In contrast, inverse analysis operates directly on measured data to construct a mathematical model that fits the data in a process called system identification. The resultant mathematical model, called the identified model, can be further employed to interpret the existing damage and predict future damage progression, a process called damage prognosis. This is when single-degree-of-freedom (SDOF) system dynamic simulations can come into play.

In this paper, a simple dynamic uniaxial mem-modeling approach is presented, that aids physical insight and enables system identification. This study begins with nonlinear system identification [22,31] and continues with dynamic simulations using a series of uniaxial models based on mem-modeling concepts and techniques.

Mem-models are a family of emerging theoretical hysteresis models, being studied by this team following the lead of [12,14] in electrical engineering, and [19,33] in mechanical engineering. Directly analyzing real-world data to substantiate the theory to facilitate similar real-world applications is what this study is about.

1.1 Background

Stress–strain datasets in this study come from an earlier laboratory study [28] which was conducted to investigate the behavior of a soft compacted clayey soil subjected to cyclic loading, part of a comprehensive investigation of the Low Track Modulus (LTM) section of the Facility for Accelerated Service Testing (FAST).

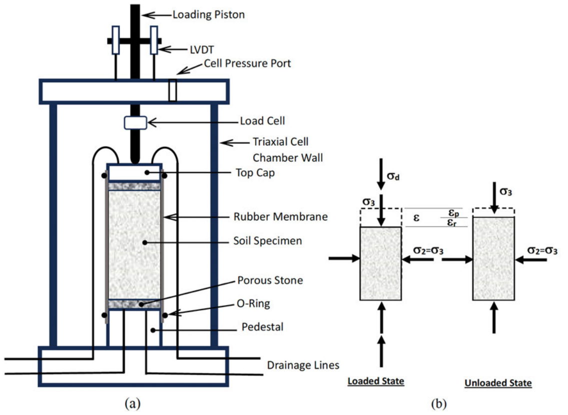

Fig. 1 **a** Schematic of cyclic triaxial testing device used by [28], and **b** schematic of stress states of cylindrical soil specimen when loaded and unloaded

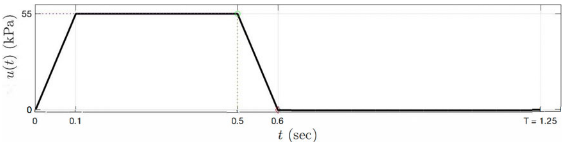

Fig. 2 Time history for one period ($T = 1.25$ seconds) of applied stress as used in the laboratory cyclic triaxial testing program of [28]

As described in [28], stress–strain data were acquired from cylindrical soil specimens that were subjected to repeated compressive loading. Figures 1 and 2 show schematics of the test setup and the profile of the compressive loading that was repeatedly applied at the top of each specimen.

The results of twelve such cyclic triaxial tests are summarized in Table 4 of [28]. The datasets are time series of the form $(t_i, \sigma_i, \varepsilon_i)$ for $i = 1, ..., N$ where t_i is time and σ_i, ε_i denote uniaxial stress and uniaxial strain (respectively) at time t_i with uniaxial meaning both quantities were measured along the cylindrical axis.

This paper presents a study of the first 200 cycles of the data acquired from Test 2 and Test 3. To highlight the richness and challenges of the selected datasets, Table 1 summarizes certain details of these tests. Test 2 reached a maximum permanent strain of 1.6% after about 15,000 cycles, which did not change much out to 72,900 cycles. Sample 2 did not experience shear failure. Test 3 resulted in rapid shear failure reaching 15% axial strain in about 800 cycles, although the loading was continued until 3250 cycles. Another important difference was that Test 2 was conducted

Table 1 Lines 1 to 7 summarize details of Tests 2 and 3, taken from [28]. Lines 8 to 13 summarize details of measured data, extracted from the first 200 cycles as part of this study

Line	Detail	Test 2	Test 3
1.	Maximum applied stress $u_{\max}$ (kPa) in Fig. 2	55	55
2.	Initial confining pressure (kPa)	14	14
3.	Initial degree of saturation, S (%)	90.4	100
4.	Drainage lines	Open	Closed
5.	Confining fluid	Air	Water
6.	Number of cycles	72,900	3,250
7.	Failed?	No	Yes
8.	Data sampling rate (Hz)	∼25	∼30
9.	Maximum strain $\varepsilon_{\max}$ (%)	∼0.9 (see Fig. 20b)	∼10 (see Fig. 3b)
10.	Maximum strain rate $\dot{\varepsilon}_{\max}$ (%/sec)	∼3 (see Fig. 21)	∼3 (see Fig. 10)
11.	Linearly regressed Young's modulus E_0 (MPa)	11.5 (see Fig. 23e)	10.8 (see Fig. 13e)
12.	Initial tangent modulus for virgin loading curve in extended Masing model E (MPa)	15–35 (see Fig. 25)	20–50 (see Fig. 16)
13.	Yield strength of virgin loading curve in extended Masing model σ_u (kPa)	25–45 (see Fig. 25)	25–35 (see Fig. 16)

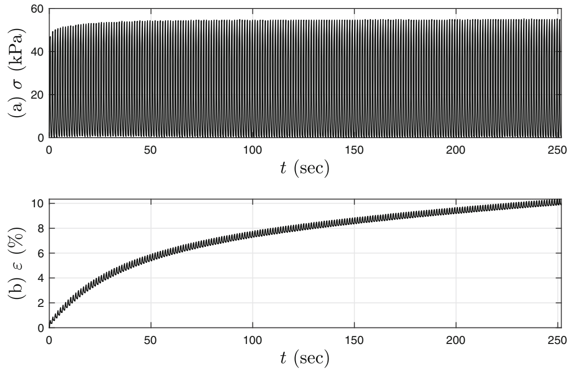

Fig. 3 Measured **a** stress and **b** strain time histories for Test 3; only the first 200 cycles are shown; the periodic loading rate is 0.8 Hz (approx)

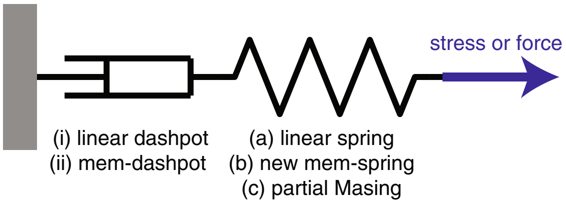

Fig. 4 Schematic of proposed serial assembly to model stress–strain or restoring force-displacement (see [40]), with (i) a linear dashpot, or (ii) a mem-dashpot capture strain/displacement ratcheting, while (a) linear spring, (b) the proposed mem-spring, or (c) partial extended Masing (minor loops only) capture the zero/origin-crossing feature. This assembly appears in Models 1 to 4 in Table 2

with the drainage lines open (pseudo-drained condition) whereas Test 3 was conducted with the drainage lines closed (undrained condition). For the latter, the development of shear-induced excess pore water pressure contributes to a rapid reduction in effective stress, which accounts for the rapid shear failure. Due to the difference in saturation and drainage conditions, the accumulated axial strain after 200 cycles was less than 1 percent for Test 2 compared to 10 percent for Test 3, as shown in Figure 5 of [28], even though both specimens were subjected to the same repeated loading. As Fig. 2 illustrates, the load applied at the top of the soil specimen during each cycle was trapezoidal in shape, increasing linearly for 0.1 s, staying constant at 55 kPa for 0.4 s, decreasing linearly to zero for 0.1 s, and then remaining at zero for 0.65 s. Hence the total period of each load cycle was 1.25 s (i.e., 0.8 Hz).

Using Test 3 as an example, Fig. 3(a and b) show the first 200 cycles of measured stress and strain versus time. A list of notation is given in Appendix A. The relevant results of Test 3 are presented in the main body of this paper while less copious Test 2 results are provided in Appendix B. The number of cycles is limited to 200, which is set for the purpose of pro-

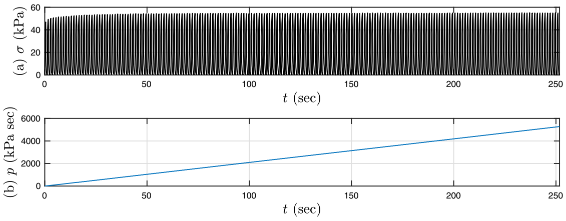

Fig. 5 Measured stress σ and integrated generated momentum p time histories for Test 3 in Panel (**a**) and (**b**), respectively

gressively developing and validating the proposed new mem-modeling approach, before eventually applying it to a greater number of load cycles.

Since only a single time series of uniaxial data are available from each test, this study focuses on the uniaxial mem-model assembly illustrated in Fig. 4, despite the fact that non-uniaxial effects (e.g., Poisson effect, shear stresses and strains) are important in cyclic triaxial tests. The purpose here is to identify the early-time stress–strain behavior of the Test 2 and Test 3 specimens not just in conventional terms, but also using recently developed mem-modeling concepts and terminology which are utilized in this work.

With constitutive modeling as our focus, we assume that the axial strain of a specimen is the change of its length divided by its original length (i.e., engineering strain). Two different modeling levels are involved: material level and system level. However geometric nonlinearities are neglected in this study, so we have simple conversions between the material and system levels. Given the dimensions of the cylindrical soil specimens in these tests with diameter $D = 2.85$ inch ($D = 7.24$ cm) and length $H = 5.21$ inch ($H = 13.2$ cm):

$$\sigma = \frac{R}{\frac{\pi D^2}{4}} \text{ in the unit of kPa} \tag{1}$$

$$\varepsilon = \frac{X}{H} \text{ in the unit of \%} \tag{2}$$

where σ and ε stand for axial stress and axial strain, respectively, while X is the displacement at the top of the specimen where the load is applied in Fig. 1 and R stands for the specimen's axial restoring force. (Wherever necessary, conversion from US customary to SI units – such as m, kPa, and % strain – are taken care of throughout this study.)

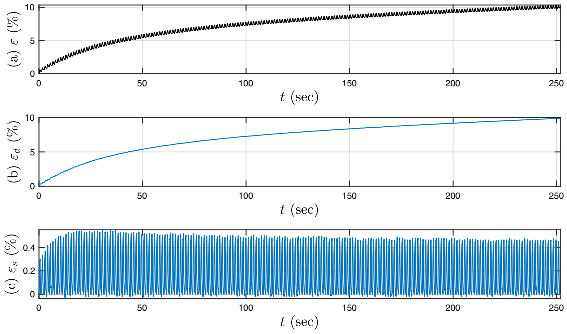

Fig. 6 **a** Measured strain ε time history for Test 3, and its two decomposed components. **b** ε_d for the mem-dashpot, and **c** ε_s for the mem-spring

1.2 Features of this study

We have two basic modeling elements in Fig. 4, damping and stiffness. As will be shown, the measured stress–strain response of each soil specimen is clearly nonlinear, which means it cannot be modeled by linear dynamics, even within a single loading cycle. Although the visual aspects of the measured stress–strain behavior, such as a hysteresis loop within each loading cycle and gradual compaction from cycle to cycle, are simple conceptually, such details are not so easily quantified in analysis nor so readily captured in programming. This was the initial challenge from the datasets in this study.

Distinct features of this study, resulting from employing mem-modeling concepts, are introduced in this subsection as a visual introduction to mem-models, before introducing mathematical expressions in the next subsection. These underlying mem-modeling concepts directly address the initial challenge, and will ultimately lead to efficient models for all simulations.

The first feature of this study is to incorporate the time integral of measured stress, called "generalized momentum" and denoted as p, in our constitutive modeling studies and as a new state variable in dynamic simulations. The background knowledge of this, which comes from bond graph theory and mem-models, will be introduced in Sect. 1.4, see Fig. 5 for the stress σ and generalized momentum p for Test 3. There is a one-to-one mapping between time t and generalized momentum p with $p(t)$ increasing monotonically as t increases. Following the ideas in [36], we will use p as an alternative means for time parameterization.

The second feature of this study is to decompose (i.e., partition) the strain time history into two parts corresponding to the two components in the model assembly as shown in Fig. 4 so that these two modeling components can be identified in a decoupled manner. Strain decomposition is part of system identification which, being an inverse mathematical problem, means that non-uniqueness issues arise. Explanation as to how the decomposition takes place will be provided under Sect. 2.1. Decomposed strain time histories are presented in Figs. 6, and 20c and d for Tests 3 and 2, respectively. Appendix C offers further justifications for the proposed signal decomposition.

Figure 6(b and c) show the decomposed strain time histories for the mem-dashpot and mem-spring, indicated by subscripts "d" and "s" and denoted by ε_d and ε_s, respectively. Hence, the decomposed strain satisfies

$$\varepsilon = \varepsilon_d + \varepsilon_s \tag{3}$$

for every measured strain value, ε_i. As will be explained in Sect. 2.1, ε_d is called the "ratcheting strain" in this study. Note that – ideally – only compression is meaningful for these tests; all measured and decomposed stresses and strains in Fig. 6 should be nonnegative, with positive meaning compression. However there are in fact a few time instants when mem-spring strains are slightly negative (i.e., tensile), which is due to small numerical errors in the decomposition, or small errors in the measured stresses and strains. Nonetheless the results of the decomposition are presented herein to reveal the usefulness of this mem-modeling approach based on the generalized momentum p and the two modeling components in Fig. 4.

The third feature of this study is to use a one-to-one mapping between the mem-dashpot strain ε_d and generalized momentum p to define the mem-dashpot. This is the signature of Dr. Leon Chua's memristor, which will be introduced in Sect. 1.4. There are one-to-one mappings for all other mem-models, as the study on mem-models continues. See Figs. 7c and 23d for the two one-to-one mappings for Tests 3 and 2, respectively. These one-to-one mappings are nonlinear functions that are easily fitted. The fitted functions will be used to represent the mem-dashpots for these two tests and used in dynamic simulations. If the fitted functions were linear (which they are not in these tests), the mem-dashpots would simply be linear viscous dampers [37,40] which is why mem-dashpots are considered generalized viscous dampers.

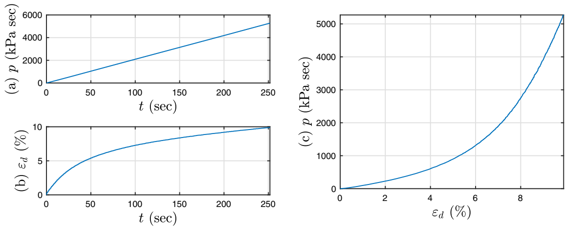

Fig. 7 **a** and **b** time histories for generalized momentum and strain for Test 3, respectively, and **c** their one-to-one mapping (i.e., parametric plot of $p(t_i)$ versus $\varepsilon_d(t_i)$, time is the common parameter)

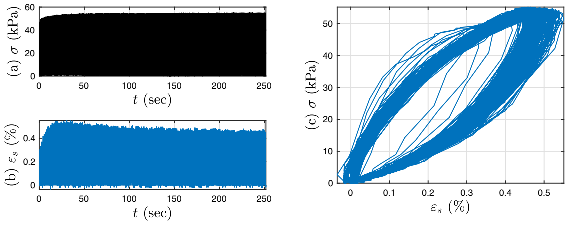

Fig. 8 **a** and **b** time histories for stress and the mem-spring strain ε_s for Test 3, respectively, and **c** their parametric plot (time is the common parameter) to reveal zero-crossing

The last feature of this study is to use a mem-spring with "zero-crossing", meaning when the mem-spring strain (with a subscript "s") is zero, the corresponding stress is (or ideally should be) zero. This is the signature of Dr. Leon Chua's memcapacitor, which will be introduced in Sect. 1.4. There are zero-crossings for all other mem-models, as the study on mem-models continues. See Figs. 8c and 23c for the mem-spring for Tests 3 and 2, respectively. These loops are not functions. The existence of these loops indicates that the underlying behavior is inelastic; i.e., mem-springs are not elastic springs.

Putting all these features together, it will be shown that the mem-dashpot captures the ratcheting strain (i.e., the accumulating strain) from cycle to cycle, whereas the mem-spring captures energy dissipation within each cycle once the ratcheting strain has been accounted for. In short, the mem-dashpot and mem-spring are devised to capture inter- and intra-cycle energy dissipation, respectively. It should be noted that in addition to the energy dissipation associated with the measured stress–strain data at the material level, the system-level model requires additional numerical dissipation in order to accomplish satisfactory nonlinear simulations. This is clarified in Appendix D.

1.3 Brief review of hysteresis modeling

Hysteresis modeling of physical systems has a long history, which dates back to the late ninteenth century in the case of magnetic materials. For a recent review of mechanical systems, see [55]; also see [30]. In [42], we examined whether mem-models could be useful for hysteresis modeling from the perspective of phenomenological modeling. In this paper, we will show that although mem-models were proposed as rate-dependent models, they can also be viewed as rate-independent models in some applications. Not to be exhaustive, rate-dependent hysteresis models include hereditary integral, e.g., [24], K-BKZ model for Alan Kaye, Barry Bernstein, Elliot Kearsley, and Louis Zapas, e.g., [29], and generalized Duhem [53]. Rate-independent hysteresis models include Preisach models [23,27,43], Prandtl – Ishlinskii model [6], Krasnosel'skii – Pokrovskii model [23], play (or backlash) and relay (or stop) [53], bilinear hysteresis [9,10], extended Masing [2,3,17,18,26], Ramberg-Osgood model [20], distributed-element model [15,16], Bouc-Wen and BWBN model [1,4,56], Duhem model [53], Leuven Model [52], and nonlinear feedback model [32,46].

1.4 Brief review of bond graph and mem-models

"Mem-models" refer to a special form of memory, i.e., hysteresis, with loading-rate dependency (which may be removed through design, e.g., [36]). Mem-models were introduced to engineering mechanics by Pei and colleagues ([36–38,40–42,54]), following the lead of [19,33]. Mem-models are based on a suite of new concepts for the memristor, memcapacitor, and meminductor developed for electrical engineering in [12,13]; revitalized since [51] and generalized in [14].

The following definitions are given at material level. System-level definitions can be easily obtained via Eqs. (1) and (2). For example, stress generalized momentum ("g-momentum" for shorthand notation) is denoted by p and is defined as follows:

$$p(t) = \int_{-\infty}^{t} \sigma(s)ds \tag{4}$$

At system level, we have generalized momentum defined as follows:

$$P(t) = \int_{-\infty}^{t} R(s)ds \tag{5}$$

where R stands for restoring force.

For the mem-dashpot at material level, we have:

$$\varepsilon_d = F_d(p_d) \tag{6}$$

where Eq. (6) is assumed to be a one-to-one mapping as mentioned previously (e.g., Fig. 7c). Differentiating Eq. (6) on both sides and applying the chain rule leads to:

$$\dot{\varepsilon}_d = W_d(p_d)\sigma_d \tag{7}$$

where $W_d(p_d) \triangleq \frac{dF_d(p_d)}{dp_d}$. When $\sigma_d = 0$, we have $\dot{\varepsilon}_d = 0$, which demonstrates the zero-crossing feature mentioned previously but for mem-dashpot.

Mem-models exploit mathematical parallelism, which needs to be handled with care [37]. The counterpart of Eq. (7) for a mem-spring is as follows:

$$\varepsilon_s = W_s(p_s)\sigma_s \tag{8}$$

which once again exhibits the zero-crossing feature but for a mem-spring (e.g., Fig. 8c). Integrating both sides of Eq. (8) with time leads to:

$$a_s = F_s(p_s) \tag{9}$$

where $W_s(p_s) \triangleq \frac{dF_s(p_s)}{dp_s}$. This demonstrates the one-to-one mapping feature described previously but for mem-spring (e.g., Fig. 13e).

Strain absement $a(t)$ is defined as the first time integral of strain:

$$a(t) = \int_{-\infty}^{t} \varepsilon(s)ds \tag{10}$$

Absement has not been often used in modeling [25]. Most recently, strain absement has been connected to damage variable in continuum damage mechanics in [42].

Strain absement at system level is defined as follows:

$$A(t) = \int_{-\infty}^{t} X(s)ds \tag{11}$$

Bond graph theory [21,34,35,44], a multi-physics theoretical framework, is where the mem-models originated. [39] studies the choices of state variables in bond graph theory, which will benefit this study.

1.5 Intended contributions and structure of this paper

The family of mem-models is a theory where the governing functional forms are abstract and to be determined per application. Aiming for real-world applications of mem-models, analyzing real-world data using these models is a necessary path. On one hand, inherent noise in real-world data measurements may cause numerical challenges so that numerical details may need to be devised to correctly and efficiently implement the theory computationally. On the other hand, analyzing real-world data offers a powerful testament and reveals new facets to the theory, literally/visually or through computation. Even though the extent and complexity will increase from analyzing simulated data, analyzing real-world data using mem-models will be a productive path.

This study expands on our preliminary prior work in [40,54] with a significantly increased scope and depth making a major leap in using real-world data to visualize mem-model concepts for teaching, and attesting the consistency of the identified mem-models using SDOF dynamic simulations to make sure that identified mem-models would perform reasonably in further damage prognosis. The former intended contribution has been described briefly in Sect. 1.2, while the latter intended contribution is detailed as follows:

First, this study validates the idea from [40,42] to design mem-models utilizing measured datasets. They include using a mem-dashpot to capture strain ratcheting in cyclic triaxial test data, and using part of an extended Masing model (minor loops only) as a mem-spring model. There are two parameters used to characterize the mem-dashpot model as in Eq. (16) for time-varying ratcheting. While two parameters are used in the adopted extended Masing model as in Eqs. (17) and (18), we will introduce six parameters as in Eqs. (19) and (20) to make the extended Masing model time-varying. Parameters for the mem-models in Fig. 4 are identified using measured data. The key signature of the mem-models is in their use of the time integral of stress and the time integral of strain.

The mem-models are then incorporated into the equation of motion and the dynamic uniaxial response of the test specimen (including inertia) is calculated for multiple cycles. This is the first time for a mem-model that has been identified using real-world datasets to then be used in dynamic simulation and validated using the same data. A series of models will be included for performance comparison, numerical validation, and physical insight; see Table 2.

The above highlights the intended contributions of this paper. In terms of presentation for both Tests 3 and 2, Sect. 2.1 summarizes the procedure for decomposing the strain, $\varepsilon(t_i) = \varepsilon_d(t_i) + \varepsilon_s(t_i)$, while Sect. 2.2 assesses the proposed decomposition in terms of strain energy dissipated during each loading cycle. Section 3.1 identifies the one-to-one mappings of the mem-dashpots for Tests 2 and 3, while Sect. 3.2 applies the extended Masing model [2,17,18] for the mem-springs not only for modeling but also for validation. Section 4 discusses simulation results and future work. Section 5 offers concluding remarks. Appendix D is a precursor to nonlinear simulation, addressing one limitation of this study. Appendix E contains all simulation details and results in this study.

Table 2 Scope of dynamic simulations in this study

Model No.	Schematic	Sec. ID	State Variables
1	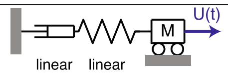	Appendix E.1	$\begin{bmatrix} P(t) \\ X(t) \end{bmatrix}$
2	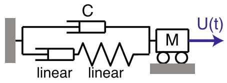	Appendix E.1	$\begin{bmatrix} P(t) \\ X(t) \end{bmatrix}$
3	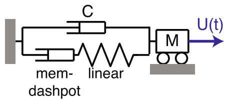	Appendix E.2	$\begin{bmatrix} P(t) \\ X(t) \end{bmatrix}$
4	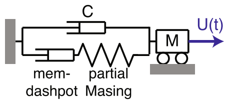	Appendix E.3	$\begin{bmatrix} P(t) \\ R(t) \\ X_s(t) \\ \dot{X}_s(t) \end{bmatrix}$

2 Data analysis using mem-model concepts

Despite the basic idea given in [40,42], the specified real-world data requires an algorithmic procedure for a correct and consistent implementation so that our work is reproducible. This entails the work under Sect. 2.1. The results from the data analysis are further examined using dissipated energy, an important physical aspect, so that the correctness of the analysis can be validated and the high quality of the selected dataset can be appreciated. This is the motivation for Sect. 2.2.

2.1 Decomposition of strain data

Figure 4 shows the model presented in [40,42] which is used throughout this study. For presentation effi-

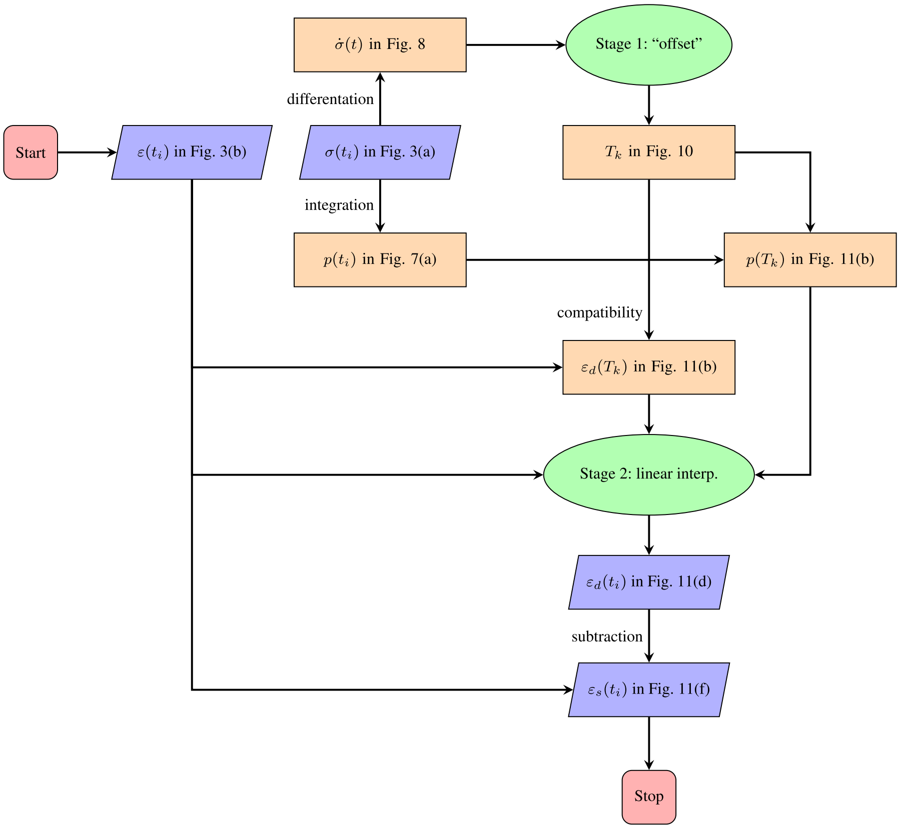

Fig. 9 Flowchart of strain decomposition using Test 3 as an example, where the two subjective decisions made are highlighted in green and links to key figures for visualization are embedded

ciency and contrasting purpose, linear dashpot and mem-dashpot occupy the slot for the dashpot, while linear spring, the proposed mem-spring, and partial extended Masing model (minor loop only), occupy the slot for the spring in the illustration. Formulations for the proposed mem-dashpot, and partial extended Masing model as mem-spring will be discussed in this paper; all model parameters will be identified using the soil data.

Serial connectivity in Fig. 4 implies additivity of strains:

$$\begin{aligned} &\varepsilon = \varepsilon_d^L + \varepsilon_s^L, \text{ for Models 1 and 2} \\ &\varepsilon = \varepsilon_d + \varepsilon_s^L, \text{ for Model 3} \\ &\varepsilon = \varepsilon_d + \varepsilon_s^M, \text{ for Model 4} \end{aligned} \tag{12}$$

where the superscript L stands for linear, while the superscript M stands for partial extended Masing model, which will be presented in Sect. 3.2 where it will be made clear that partial extended Masing model is a mem-spring.

Focusing on mem-dashpot and mem-spring in series, the modeling elements labelled as (ii) and (c) in Fig. 4, Eqs. (6) and (8) are applied, respectively. In addition, serial connectivity implies stress equality $\sigma_d = \sigma_s = \sigma$, and consequently $p_d = p_s = p$, so that Eq. (12) becomes:

$$\varepsilon = F_d(p) + W_s(p)\sigma \tag{13}$$

which is identified using the method given in [40]: Theoretically, when $\sigma = 0$, we have $\varepsilon_s = W_s(p)\sigma = 0$. Equivalently, when $\sigma = 0$, we have $\varepsilon = \varepsilon_d$. Procedurally, cycle separation times $T_1 < T_2 < T_3 \ldots$ corresponding to $\sigma(T_k) = 0, k \in \mathbb{Z}^+$ are identified first. Next, identify F_d for the mem-dashpot using $\varepsilon_d(T_k) = F_d(p(T_k))$. Last, identify the residue as the mem-spring. This is the basic idea given in [40,42].

To carry out this simple idea, thorough examinations of the data, careful thinking, and numerical treatments were needed; see the detailed flowchart in Fig. 9 with embedded links to key figures to illustrate numerical challenge and proposed numerical treatment.

Subjective decisions take place in two stages as illustrated in Fig. 9, where approximation errors propagate. Stage 1 involves decomposing the strain history into load cycles defined by the time instants T_k by choosing the value for "offset". See Fig. 10a and b for typ-

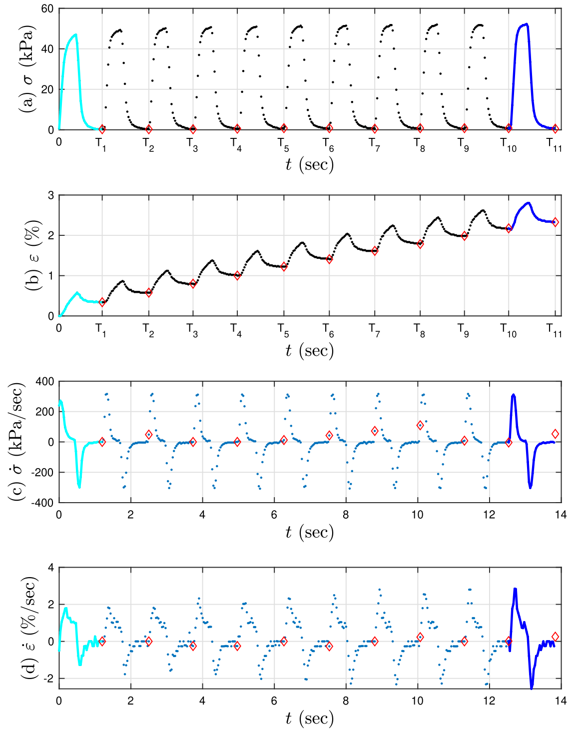

Fig. 10 Time histories of the first 11 cycles of Test 3 dataset, where the first and 11th cycles are highlighted in cyan and blue, respectively, and the red diamonds are separation points for strain decomposition with an offset value of 3: **a** and **b** measured stress and strain time history, respectively, where the cycle separation time instants $T_1 < T_2 < T_3 \ldots < T_{11}$ are marked, and **c** and (d) numerically differentiated stress and strain rate time history, respectively

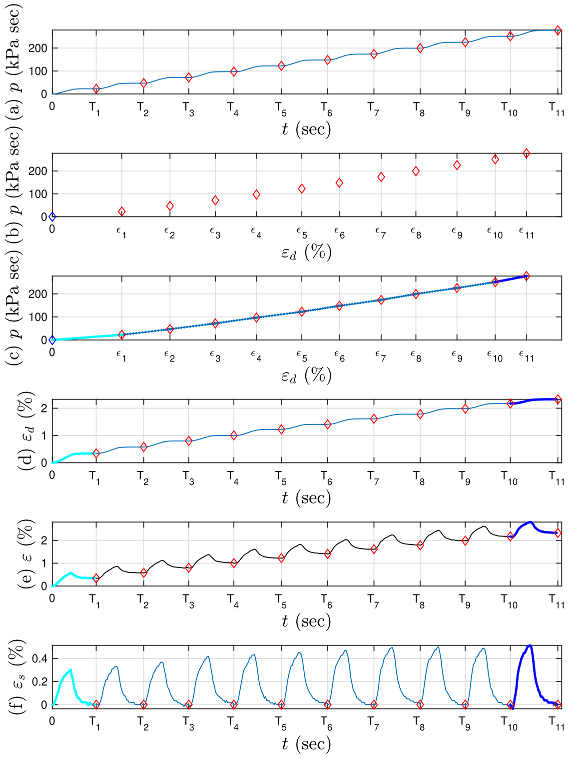

Fig. 11 Time histories of the first 11 cycles of Test 3 dataset, where the first and 11th cycles are highlighted in cyan and blue, respectively, and the red diamonds are separation points for strain decomposition with an offset value of 3: **a** integrated generalized momentum p time history, **b** the identified $\varepsilon_d(T_k)$ and $p(T_k)$ pairs plus the origin, **c** the piecewise linearly interpreted $p - \varepsilon_d$, **d** the obtained ε_d time history, **e** the measured strain ε time history, and **f** the obtained ε_s time history

ical zoomed-in views of measured time histories of stress and strain, where plateaus around zeros and local minima can be seen for stress and strain, respectively. These are the numerical details that are simple conceptually but not so easily quantified numerically. To capture cycle separation time instants T_k numerically, local peaks in $\dot{\sigma}$ are identified first, followed by determining offset values empirically. Results of a study of offset values in Stage 1 are presented in Appendix C; the empirically determined offset values are 2 and 3 for Tests 2 and 3, respectively. We apply the MATLAB code central_diff.m [8] to ensure forward and backward differences at the left and right ends, respectively, and with the same second-order of accuracy as the central difference for the mid-portion.

Stage 2 involves decomposing the measured strain history data within each cycle into mem-dashpot and mem-spring strains; see Fig. 11. The residue for the mem-spring is obtained by first fitting the mem-dashpot, $\varepsilon_d(t_i) = F_d(p(t_i))$, using simple linear interpolation (interp1 in MATLAB). The identified mem-spring is not as accurate as the dashpot.

The mem-dashpot strain at the end of each cycle $\varepsilon_k = \varepsilon_d(T_k)$ is called the "ratcheting strain" in this study because physically the reduced length of the soil specimen at the k-th cycle is determined by ε_k. In Fig. 11b, the red diamonds indicate points (ε_k, p_k) but no curve connecting these points is shown, which is the status of strain decomposition at the end of Stage 1. Figure 11c shows these points connected by straight lines which is a consequence of assuming and imposing piecewise linear interpolation in Stage 2.

Returning to Fig. 6, panel (b) shows the ratcheting strain $\varepsilon_d(t_i)$ for the first 200 cycles while panel (c) shows the remaining part of the strain that is attributed

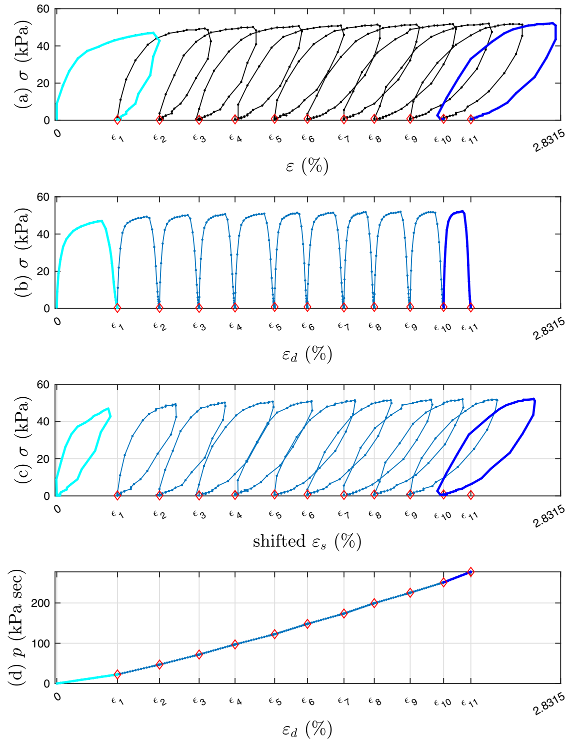

Fig. 12 **a**–**c** Hysteresis loops, and **d** one-to-one mapping of the first 11 cycles of Test 3 dataset, where the first and 11th cycles are highlighted in cyan and blue, respectively, and the red diamonds are separation points for strain decomposition with an offset value of 3, where 11 values of $\varepsilon = \varepsilon_d$ are marked with the corresponding $\varepsilon_s = 0$: **a** measured stress–strain curve; **b** decomposed stress–strain for the underlying mem-dashpot model; **c** decomposed stress–strain for the underlying mem-spring model, and **d** stress time integral-strain time integral for Panel (c)

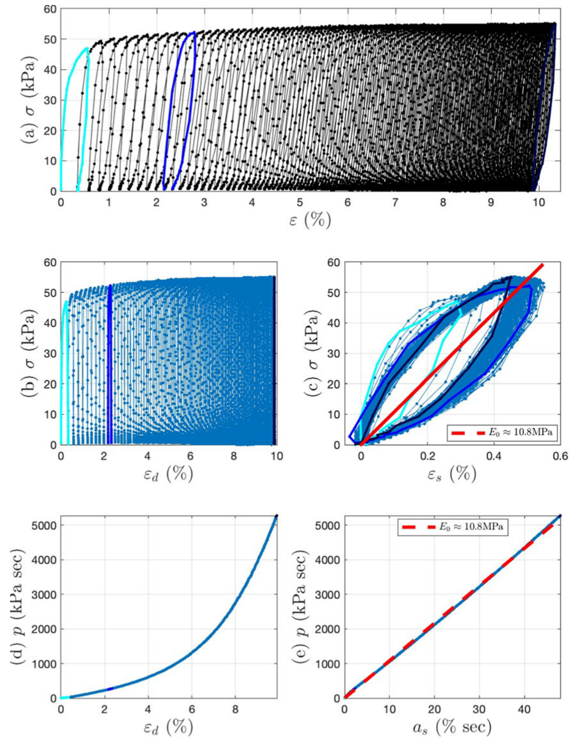

Fig. 13 **a**–**c** Hysteresis loops, and **d** and **e** one-to-one mappings of the first 200 cycles of Test 3 dataset, where the first, 11th (the largest) and last (the smallest) cycles are highlighted in cyan, blue, and dark blue, respectively, with a strain decomposition with an offset value of 3: **a** measured stress–strain curve; **b** and **c** decomposed stress–strain relations for the underlying mem-dashpot and mem-spring as in Fig. 4, respectively, and **d** and **e** the input–output one-to-one mappings for **b** and **c**, to define the mem-dashpot and mem-spring, respectively

to the mem-spring; i.e., $\varepsilon_s(t_i) = \varepsilon(t_i) - \varepsilon_d(t_i)$. Note that the vertical scales of panels (b) and (c) in Fig. 6 differ by a factor of 20.

Figure 12 shows hysteresis loops (stress versus strain) using the decomposed strains. Decomposed stress–strain curves and their corresponding one-to-one mappings for Test 3 are presented in Fig. 13; the counterpart for Test 2 is presented in Fig. 23.

These outcomes of the proposed decomposition make sense intuitively: Figs. 12a and 13a display repetitive stress–strain loops, all of which appear to anchor around their lower left corners. The anchor points do not remain in one place. Rather, they seem to drift from cycle to cycle. These observations are about the periodicity, and inter-cycle strain ratcheting in the data. These repetitive loops are not stationary; intra-cycle gradual densification is the cause. The proposed decomposition thus assists quantitative data analysis with physical insights, creating an algorithmic procedure that would be hard to reason otherwise.

What will follow is how to identify these two modeling components independently as in Sect. 3. Before getting there, we will examine dissipated energy before and after the decomposition to validate the implemented decomposition and appreciate the high quality of the selected datasets.

2.2 Dissipated energy

Energy (per unit volume) dissipated by the specimen during the kth loading cycle, D_k, is defined as:

$$D_k = \int_{T_k}^{T_{k+1}} \sigma(t) d\varepsilon(t) \tag{14}$$

Table 3 Details of estimated energy (per unit volume) D_k dissipated during the kth cycle for Test 3; see Fig. 12a

Cycle n. k	Index i_b	Index i_e	T_k (sec)	ε (%)	D_k (J/m^3)
1	1	37	1.2000	0.3409	184.0334
2	37	76	2.5000	0.5774	168.1251
3	76	113	3.7330	0.8000	169.9906
4	113	150	4.9670	1.0017	178.0853
5	150	189	6.2670	1.2243	178.7751
6	189	227	7.5330	1.4087	179.3887
7	227	265	8.8000	1.6139	177.3015
8	265	303	10.0670	1.7843	182.0625
9	303	340	11.3000	1.9861	185.9214
10	340	377	12.5330	2.1739	178.1904
11	377	416	13.8330	2.3270	181.6914

where T_k and T_{k+1} are the identified beginning and end times (respectively) of the kth cycle with $k = 1, 2, 3, \ldots, 199$. D_k is estimated in this study using the trapezoidal rule:

$$D_k = \sum_{i=i_b}^{i=i_e} \frac{1}{2} \left(\sigma_i + \sigma_{i+1}\right) \left(\varepsilon_{i+1} - \varepsilon_i\right) \tag{15}$$

where i is the index of the time series $(t_i, \sigma_i, \varepsilon_i)$ where $i = i_b, i_{b+1}, \ldots i_e$ is the kth cycle, with i_b and i_e being the beginning and end index, respectively. Table 3 gives computational details of D_k for Test 3, associated with Fig. 12a, while Fig. 14 presents the dissipated energy not only for the specimen but also for the two decomposed components (i.e., mem-dashpot and mem-spring) since $\varepsilon = \varepsilon_d + \varepsilon_s$. The counterparts for Test 2 are Table 6 and Fig. 24. It is interesting to observe the (automatically) identified values T_k in these two tables: According to Fig. 2, the increment of T_k from cycle to cycle should be constant – equal to the period $T = 1.25$ seconds – but in fact these increments deviate somewhat from this value, a vivid reminder of the noisiness inherent in all real-world data.

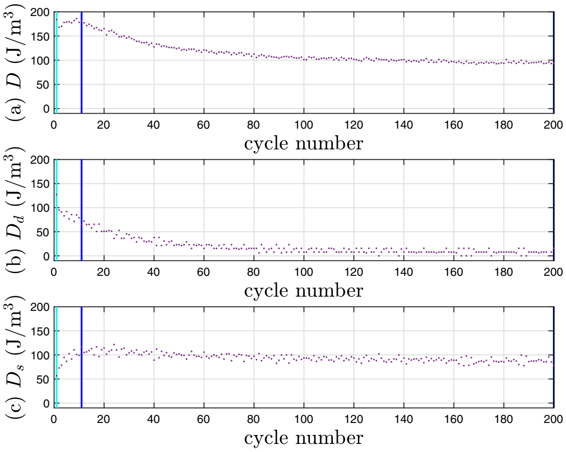

Fig. 14 Dissipated energy (per unit volume) for each load cycle: **a** D_k for Test 3, **b** D_d for the mem-dashpot, **c** D_s for the mem-spring, where cycle numbers 1, 11 and 200 are highlighted in cyan, blue, and dark blue, respectively

Table 4 Mem-dashpot parameters ε_0 and p_0 obtained by fitting hyperbolic curve Eq. (16) using first 200 cycles of test data

Test	2	3	Unit
ε_0	1.05	12.5	%
p_0	950	1,400	kPa-sec

In both tests, the energy dissipated during each load cycle D_k is always positive, fluctuating somewhat from cycle to cycle. Positive D_k for each k is to be expected since the soil specimen was intentionally stressed beyond its elastic limit during each cycle. In Test 2, D_k decreases somewhat as k increases, with the mem-spring dissipated energy D_s being nearly 100 percent of the dissipated energy per cycle compared to the mem-dashpot dissipated energy D_d. We note here that $D_k = D_d + D_s$ for each cycle because the strain decomposition satisfies $\varepsilon = \varepsilon_d + \varepsilon_s$ for each time t_i. However slightly negative values of mem-dashpot dissipated energy were noted at a few time points t_i for Test 2, due to the fact that the strain decomposition of Test 2 is numerically more sensitive than Test 3.

3 Identified mem-models

3.1 Two mem-dashpot models

As shown in Fig. 13d, the one-to-one mapping for the mem-dashpot labelled as Item (ii) in Fig. 4, is clearly nonlinear. Hyperbolic curve fitting following Eq. (16) is applied to it; the results of the two identified parameters, ε_0 and p_0, are given in Table 4.

$$\varepsilon_d = F_d(p) = \varepsilon_0 \frac{\left(\frac{p}{p_0}\right)}{\left[1 + \left(\frac{p}{p_0}\right)\right]} \tag{16}$$

We take a moment to examine Eq. (16), in which the variable p appears in a normalized form, $\frac{p}{p_0}$. Given this functional form, each parameterized mem-dashpot model is loading-rate independent, although mem-dashpots are loading-rate dependent models. Moreover, strain ratcheting is known to be a loading-rate dependent phenomenon. For our purposes, Eq. (16) works for each test simply by using different values of p_0 and ε_0.

Even though cyclic stress–strain behaviors in these compression tests are complex, the proposed model assembly in Fig. 4 is relatively simple and each modeling element is intended to be defined by a relatively simple nonlinear static one-to-one function such as the hyperbolic curve with two parameters for the mem-dashpot. This manifests one of the key aspects of our mem-modeling approach to these test data.

3.2 Minor loops of extended masing model for mem-springs

Looking next at Panel (e) in Fig. 13, the Test 3 one-to-one mapping for the mem-spring is (or at first glance seems to be) a straight line. A linear regression result is presented using a red dashed line for the discrete pairs of (a_s, p) with a slope of $E_0 \approx 10.8$ MPa. Referring to [38], we have $\frac{\sigma}{\varepsilon_s} = \frac{dp}{da_s}$, meaning that the secants of the stress–strain loops in Panel (c) are equal to the corresponding tangents of generalized momentum-absement curve in Panel (e). E_0 is thus also drawn in a red dashed line in Panel (c), representing the identified average Young's modulus of the stress–strain loops, an insightful concept that will be followed up on momentarily.

The extended Masing model (presented herein) follows [2,17,18]. The virgin loading curve starts with one particularly simple functional form proposed in Eq. (5.29) in [17] so that the expressions for minor loops are as follows - specifically for this study, among all equivalent options:

$$\dot{\sigma}_M = E\left(1 - \frac{\sigma_M - 0}{2\sigma_u}\right)\dot{\varepsilon}_M, \quad \text{loading reloading (this study)} \tag{17}$$

$$\dot{\sigma}_M = E\left(1 - \frac{\sigma^* - \sigma_M}{2\sigma_u}\right)\dot{\varepsilon}_M, \quad \text{unloading (this study)} \tag{18}$$

where E stands for the initial tangent modulus for the virgin loading curve and all unloading and reloading curves. Whereas σ_u is the yield strength for the virgin loading curve, $2\sigma_u$ is the yield strength for all minor loops following the Masing rule reviewed in [3]. σ^* is the stress at the pivoting point where $\dot{\varepsilon}_M = 0$ and $\dot{\sigma}_M = 0$ simultaneously. There are three independent parameters, σ_u, E, and n in [17], however we use $n = 1$ in this study for simplicity.

The idea of using minor loops of extended Masing model to model the mem-spring is given in [40,42]. Figure 15 presents individual approximations of three typical mem-spring loops from load cycles 1, 11 and 200. Note either a loading/reloading or unloading branch is needed to identify the two parameters, σ_u and E. Both the loading/reloading and unloading branches could be used for the identification, further leading to averaged results. The key message here, however, is that both σ_u and E values vary from cycle to cycle. Figure 16 further presents both σ_u and E values for all 200 cycles. Using extended Masing models for individual loops is thus inadequate. The proposed mem-spring addresses this modeling need. [11] proposes a deteriorating Masing, however the approach differs from this study.

This study enriches the extended Masing model using either absement or generalized momentum to approximate σ_u and E. This means that the cycle numbers in Fig. 16 can be replaced with their corresponding either absement a or generalized momentum p, with the latter choice leading to Fig. 17.

See Fig. 17 first for identified and normalized σ_u and E, each plotted as a function of p. Recall [36] points out that absement and generalized momentum introduce means for time parameterization. For this study, we use the following normalized fits:

$$\overline{\sigma}_u = a_1 - \exp\left(a_2 \frac{p}{\max(p)} + a_3\right) \tag{19}$$

$$\overline{E} = b_1 + \exp\left(b_2 \frac{p}{\max(p)} + b_3\right) \tag{20}$$

so that we apply Eqs. (19) and (20) to obtain $\sigma_u = \overline{\sigma}_u \max(\sigma)$ and $E = \overline{E}\frac{\max(\sigma)}{\max(\varepsilon_s)}$, respectively. See Fig. 17 also for the fitted results of Test 3. Table 5 gives identified parameters for both Tests 2 and 3.

The identified average modulus E_0 is marked in both Figs. 15 and 16 so that the value of E at the start of

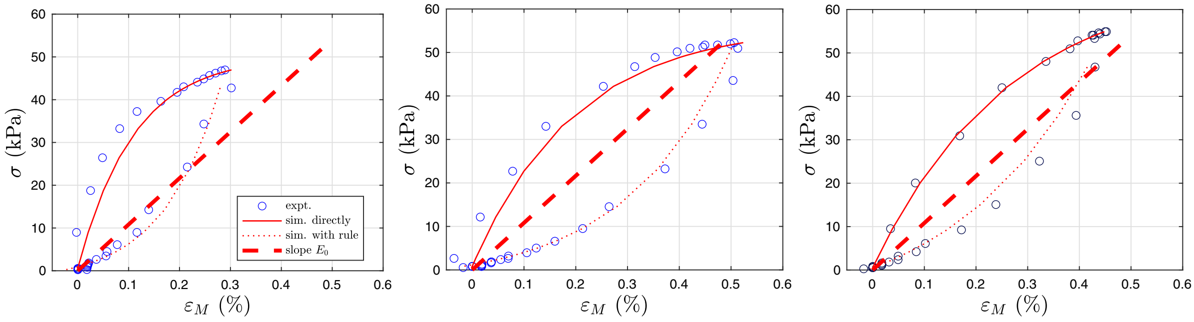

Fig. 15 Experimental data in Test 3 decomposed with an offset of 3 in contrast with fitted curve directly from using one particularly simple functional form [17] and from applying Masing rule: From left to right, the first, 11th, and 200th cycles

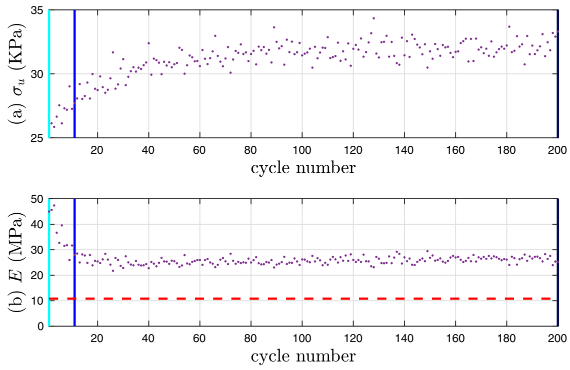

Fig. 16 Results of identified σ_u and E from all loading/reloading branches of Test 3 with an offset of 3, and the identified value of E_0

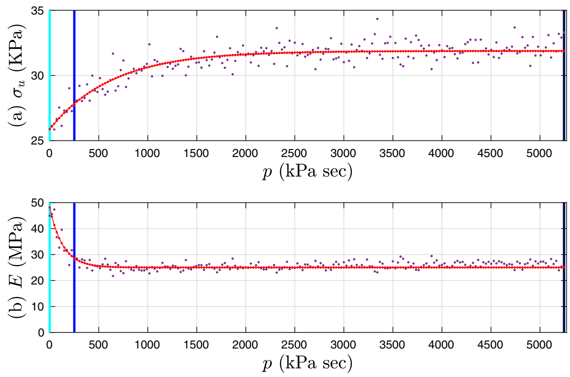

Fig. 17 Results of identified σ_u and E from all loading/reloading branches of Test 3 with an offset of 3, and those from applying Eqs. (19) and (20) with the identified parameter values given in Table 5

Table 5 Parameter values from normalized fit using Eqs. (19) and (20). †at 200 cycles

Test†	a_1	a_2	a_3	b_1	b_2	b_3
2	0.9738	-0.0328	-0.3914	1.8337	0.2656	-1.0895
3	0.2889	-8.2269	-2.9120	2.5004	-38.6961	0.8370

each cycle can be compared with the average value E_0. Since the initial slope of a stress–strain loop is the maximum tangent modulus of that loop, comparison of E and E_0 in both Figs. 15 and 16 quantifies the maximum stiffness of the soil specimen during each cycle (as compared to the linear spring). A proper stiff solver will be adopted later.

4 Discussion of simulation results and future work

Referring to Appendix E, where full-system dynamical simulation method, details, results and discussions using Models 1 to 4 under Table 2 are presented, gradual improvements in comparison with the experimental measurements are shown from model to model due to the introduced mem-dashpot and mem-spring. Only Figs. 18 and 19, selected results from Model 4, are included in the main text.

Different types of parametric plots are useful in mem-modeling. For example, Fig. 18 has five different parametric plots, each of which presents results from Model 4 simulations overlaid with corresponding measured data for the first 200 cycles whereas Fig. 19 shows the same plots for the first 11 cycles. Panel (a) in those two figures show parametric plots of stress versus strain, a type of plot that is commonly used to display hysteresis loops. Less common are panels (d) and (e), both of which show one-to-one mappings that are fundamental in this study. In Fig. 18d, the plot of

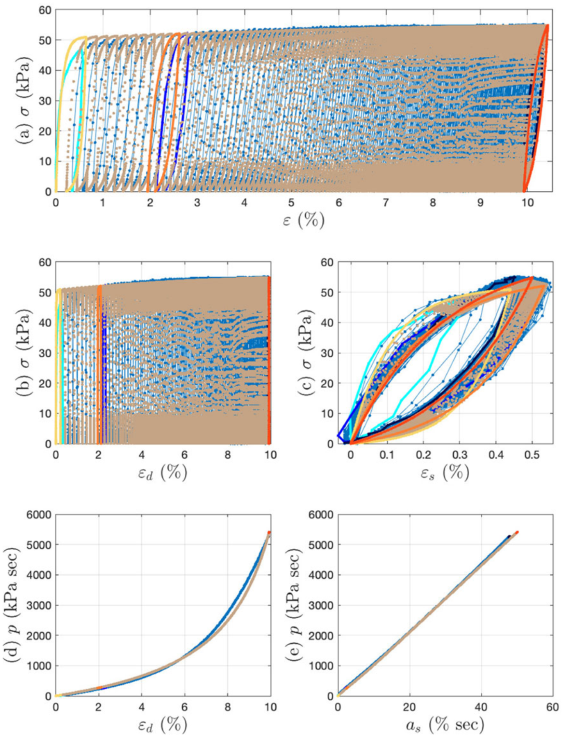

Fig. 18 **a–c** Hysteresis loops, and **d** and **e** one-to-one mappings of the first 200 cycles of Test 3 dataset in pale blue, where the first, 11th and 200th cycles are highlighted in cyan, blue, and dark blue, respectively, overlaid with the full-system simulation results in brown, where the first, 11th, and 200th cycles are highlighted in yellow, orange and dark orange, respectively. Model 4 in Table 2 is adopted with $\zeta = 4$. The "event option" under MATLAB ode15s is used with AbsTol $= 10^{-12}$, RelTol $= 10^{-3}$, and Refine $= 1$

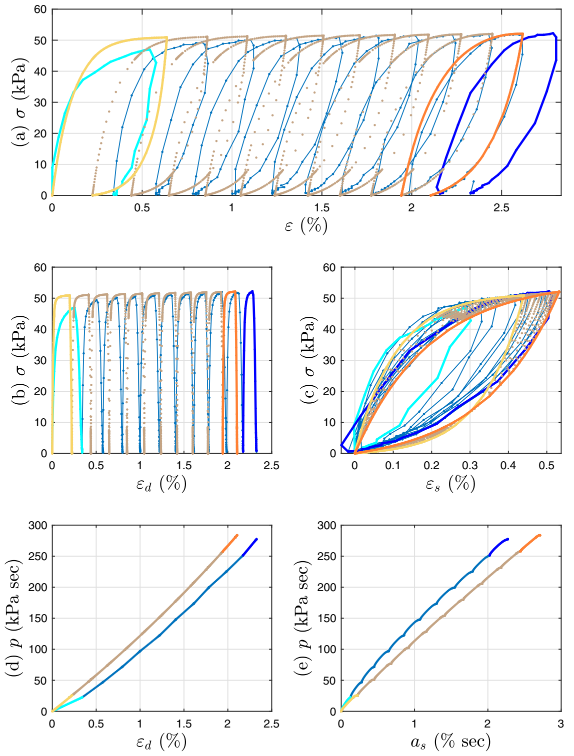

Fig. 19 **a–c** Hysteresis loops, and **d** and **e** one-to-one mappings of the first 11 cycles of Test 3 dataset in pale blue, where the first and 11th cycles are highlighted in cyan and blue, respectively, overlaid with the simulation results in brown, where the first and 11th cycles are highlighted in yellow and orange, respectively. Model 4 in Table 2 is adopted with $\zeta = 4$. The "event option" under MATLAB ode15s is used with AbsTol $= 10^{-12}$, RelTol $= 10^{-3}$, and Refine $= 1$

generalized momentum p versus ratcheting strain ε_d indicates that the mem-dashpot captures a significant part of the nonlinear response of the soil specimen over the course of 200 cycles; similarly the plot of p versus mem-spring absement a_s in Fig. 18e shows that the mem-spring captures most of the remaining nonlinear response during 200 cycles. However Figs. 19d and e indicate that additional modeling effort would be required to improve the first 11 cycles.

Both Figs. 14 and 24 indicate the dominance of the mem-springs for the dissipated energy, calling for continued effort to advance mem-spring models. To enrich the extended Masing model with the mem-model concepts, $n = 1$ is fixed in this study for model simplicity but other n values could be explored.

For SDOF dynamic simulations concerning the selected datasets, it remains to be seen if incorporating geometric nonlinearity would be fruitful. Another idea is to replace the linear viscous damper for numerical damping in Models 2 to 4 in Table 2 with a mem-dashpot. This is because this numerical damping may be displacement-dependent, i.e., a mem-dashpot. Multi-degree-of-freedom (MDOF) dynamic simulations using identified mem-models are to be investigated too. These are among the future work that we envision.

A separate comprehensive investigation should also be undertaken to study how the quality of (i.e., excessive noise in) experimental data would affect the identified mem-models and SDOF and MDOF dynamic simulations.

Last but not least, correlating relevant material properties with the parameters in the mem-models, i.e., the two in Eq. (16) for time-varying ratcheting, and six in

Eqs. (19) and (20) for time-varying extended Masing model, calls for future studies to reveal both statistical patterns and physical insights.

5 Concluding remarks

This study has introduced the mem-models to geotechnical engineering applications using two published datasets. The selected case study is challenging due to modeling time-varying systems. Two mem-models, mem-dashpot and mem-spring, have been devised in series to capture time-varying ratcheting and densification, respectively, in cyclic responses. Both identification (inverse problem) of the model parameters and simulation (forward problem) using the identified models have been carried out in this study.

To complement the existing theoretical foundation, a numerical procedure has been proposed for strain signal decomposition, leading to quantification of an otherwise hard-to-quantify significant physical insight. This aspect of the work alone contributes to a tool for visualization and data analysis. Modeling physical attributes in a decoupled manner is a leading feature of this work.

This study has substantiated both problem formulation and key numerical simulation details to benefit SDOF dynamic simulations using mem-models. Bond graph theory has been used to choose state variables; state event location algorithm and a stiff solver are used to solve piecewise smooth dynamics.

This study has greatly benefited from full time history measurements of high quality. The selected datasets have been used to effectively teach the abstract concepts in mem-models. A suite of comparative models have been employed for contrast and comparison purpose to appreciate the great benefit from using time integrals of stress and strain as in mem-dashpots and mem-springs, opening the door to many other similar and more challenging real-world applications involving modeling of hysteresis.

Acknowledgements Jin-Song Pei, Joseph P. Wright, and Marco B. Quadrelli acknowledge the Oklahoma NASA EPSCoR for the Faculty Research Initiation Fellowship that initiated this study. Government sponsorship acknowledged. Dr. Marco Quadrelli's research was carried out at the Jet Propulsion Laboratory, California Institute of Technology, under a contract with the NASA Aeronautics and Space Administration. Jin-Song Pei and Francois Gay-Balmaz acknowledge the NSF project BRITE Relaunch 2227495 that completed this study. The authors appreciate one of the anonymous reviewers to improve the clarity of the presentation, and the other to suggest future work to study the effect of excessive noise in experimental data.

Author contributions J.S. Pei processed the data and wrote the main manuscript. J.P. Wright provided critical physical insights and numerical solution, and made major revisions of the manuscript. G.A. Miller provided the data and explained all technical aspects of the data. F. Gay-Balmaz reviewed the manuscript. M.B. Quadrelli suggested the specified application of mem-modeling.

Funding The authors have not disclosed any funding.

Data availibility The experimental data used in this study will be made available through https://osf.io/phzs9/. Further requests should be addressed to Jin-Song Pei.

Declarations

Conflict of interest The authors declare that they have no conflict of interest.

A Notation

a	Strain absement, first time integral of strain ε
b	Subscript to be used with index i for "beginning"
d	Subscript to be used with strain ε, one-to-one mapping F, and dissipated energy D for "dashpot"
e	Subscript to be used with index i for "ending"
i	Index
k	Dummy index for cycle number
n	Power term in extended Masing model
t	Time
p	Generalized momentum, the first time integral of σ
p_0	Coefficient used to normalize p in fitting mem-dashpot's one-to-one mapping
u	Applied stress
$\mathbf{y}$	State variables

A	Absement, first time integral of displacement X
C	Damping coefficient of linear numerical damper in Models 2 to 4
D	Dissipated energy per unit volume
D	Diameter of soil specimen
E	Initial tangent modulus for virgin loading curve in extended Masing model
E_0	Linearly regressed Young's modulus of soil stress-strain loops
F	One-to-one mapping for mem-model in an effort-controlled setting
H	Height of soil specimen
K	Stiffness of soil specimen
L	Superscript to be used with strain ε for "Linear"
M	Mass of soil specimen
M	Superscript to be used with strain ε for "Masing"
N	Length of a dataset
P	Generalized momentum, the first time integral of R
R	Restoring force of soil specimen
W	Secant stiffness function in a stress-controlled mem-spring model
U	Applied force to soil specimen
V	Volume of soil specimen
X	Displacement at soil specimen's top
ε	Strain
ε_0	Coefficient used to normalize ε_d in fitting mem-dashpot's one-to-one mapping
ρ	Density of soil specimen
σ	Stress
σ_u	Yield strength of virgin loading curve in extended Masing model
τ	Relaxation time for linear damper in Models 1 and 2
ζ	Damping ratio of linear numerical damper in Models 2 to 4

B Results of test 2

See Table 6, and Figs. 20–26.

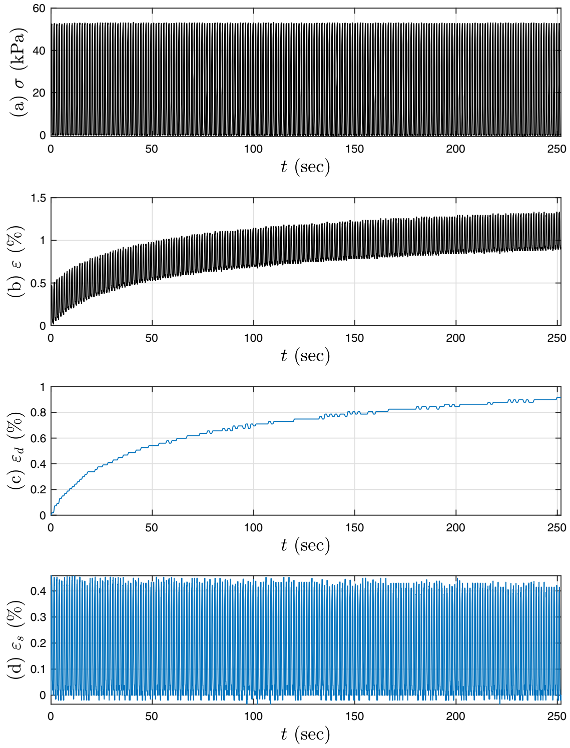

Fig. 20 Measured time histories in Panels **a** and **b** to be used in this study, together with decomposed ones with an offset of 2 in Panels **c** and **d** for Test 2

Table 6 Details of estimated energy (per unit volume) D_k dissipated during the kth cycle for Test 2; see Fig. 22

Cycle no. k	Index i_b	Index i_e	T_k (sec)	ε (%)	D_k (J/m^3)
1	1	31	1.2000	0.0192	97.2572
2	31	62	2.4400	0.0729	106.2925
3	62	94	3.7200	0.0921	98.0569
4	94	125	4.9600	0.1305	97.1784
5	125	156	6.2000	0.1497	92.1115
6	156	188	7.4800	0.1689	95.2087
7	188	219	8.7200	0.1881	92.6572
8	219	251	10.0000	0.2073	94.8052
9	251	282	11.2400	0.2226	92.4610
10	282	314	12.5200	0.2418	94.0875
11	314	345	13.7600	0.2610	90.7621

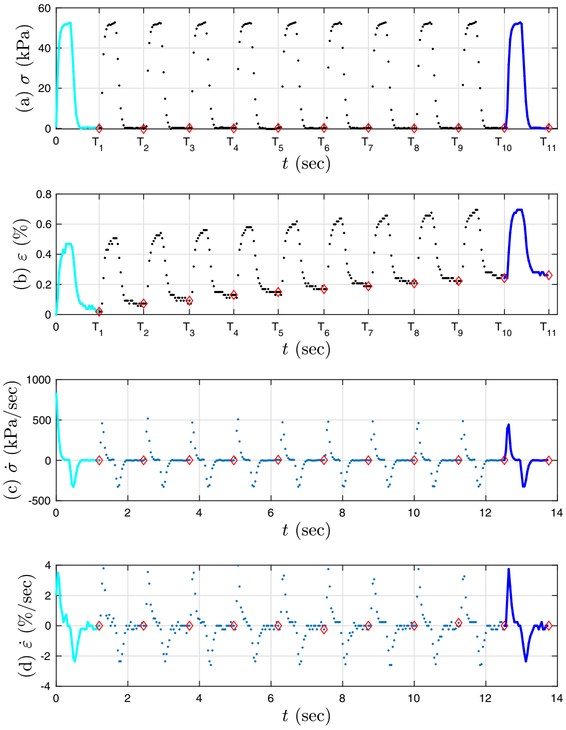

Fig. 21 Time histories of the first 11 cycles of Test 2 dataset, where the first and 11th cycles are highlighted in cyan and blue, respectively, and the red diamonds are separation points for strain decomposition with an offset value of 2: **a** and **b** measured stress and strain time history, respectively, where the separation time instants $T_1 < T_2 < T_3 \ldots < T_{11}$ are marked, and **c** and **d** numerically differentiated stress and strain rate time history, respectively

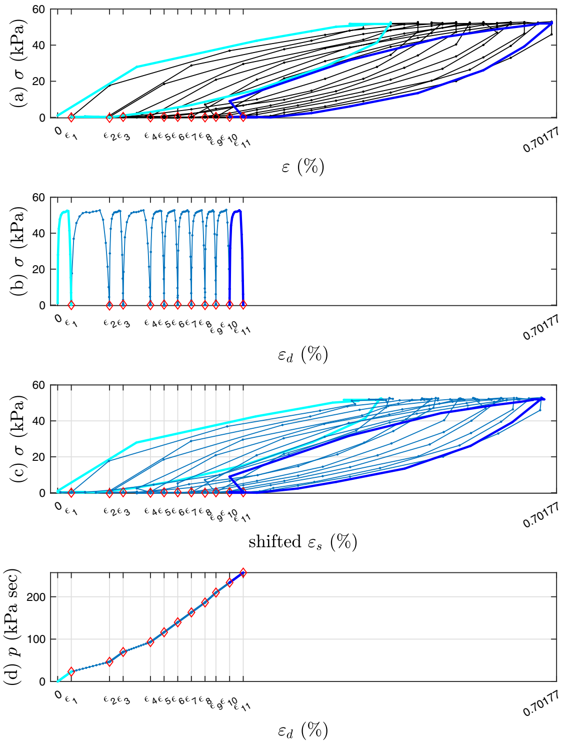

Fig. 22 **a**–**c** Hysteresis loops, and **d** one-to-one mapping of the first 11 cycles of Test 2 dataset, where the first and 11th cycles are highlighted in cyan and blue, respectively, and the red diamonds are separation points for strain decomposition with an offset value of 3, where 11 values of $\varepsilon = \varepsilon_d$ are marked with the corresponding $\varepsilon_s = 0$: **a** measured stress–strain curve; **b** decomposed stress–strain for the underlying mem-dashpot model; **c** decomposed stress–strain for the underlying mem-spring model, and **d** stress time integral-strain time integral for Panel **c**

C More on decomposition

Alternative decomposition schemes were tried in this study, for example, detecting the valleys of either $\sigma(t)$ or $\varepsilon(t)$. These decomposition results, using matlab command find, also depended on the values of the governing parameters. They were not guaranteed to lead one separation point per cycle, thus not adopted in this study.

Selected effect of the proposed offset values is presented in Figs. 27 and 28 for Tests 3 and 2, respectively.

D Linear dynamic maxwell simulations

Before embarking on mem-model simulations, linear dynamic Maxwell simulations were conducted using

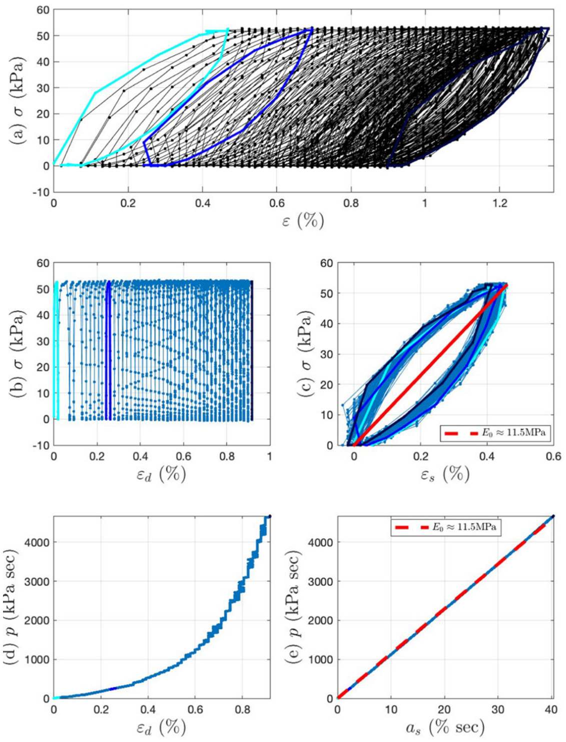

Fig. 23 **a**–**c** Hysteresis loops, and **d** and **e** one-to-one mappings of the first 200 cycles of Test 2 dataset, where the first, 11th (the largest) and last (the smallest) cycles are highlighted in cyan, blue, and dark blue, respectively, with a strain decomposition with an offset value of 2: **a** measured stress–strain curve; **b** and **c** decomposed stress–strain relations for the underlying mem-dashpot and mem-spring as in Fig. 4, respectively, and **d** and **e** the input–output one-to-one mappings for **b** and **c**, to define the mem-dashpot and mem-spring, respectively

Table 7 Young's modulus E_0 and relaxation time τ used in linear dynamic Maxwell simulations

Test	2	3	Unit
E_0	11.5	10.8	MPa
τ	10	1	sec

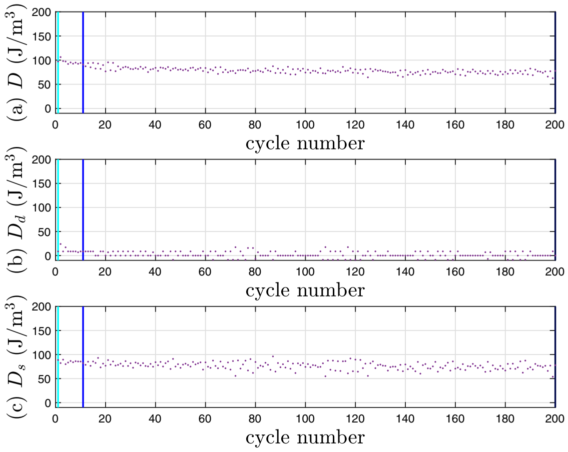

Fig. 24 Dissipated energy evolution for **a** the mem-dashpot, **b** the mem-spring, and **c** the total for Test 2, where the first, 11th (the largest) and 200th (the smallest) cycles are highlighted in cyan, blue, and dark blue, respectively

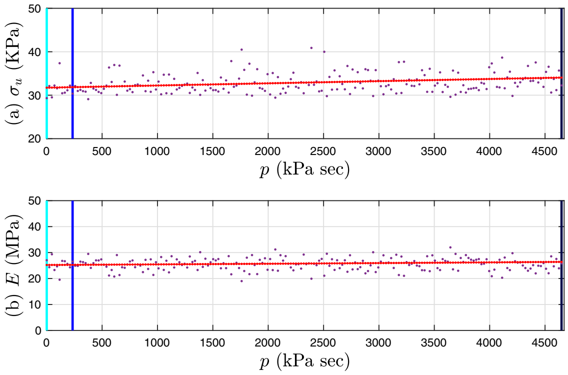

Fig. 25 Results of identified σ_u and E from all loading/reloading branches of Test 2 with an offset of 2, and those from applying Eqs. (19) and (20) with the identified parameter values given in Table 5

the two linear dynamic Maxwell systems subjected to the trapezoidal loading shown in Fig. 2. A key result from this part of our study is that a substantial amount of additional energy dissipation per load cycle (beyond the measured dissipated energy D_k) is needed when using this simple dynamic uniaxial model. This additional dissipation (in the form of a linear viscous damper) is even more important when conducting nonlinear (mem-model) simulations involving hundreds of load cycles. The modeling elements and their connectivities are identical to those in Models 1 and 2 in Table 2, respectively, however the choices of state variables differ. Conventional choices of state variables are exercised here for reference, while those suggested by bond graph theory are exercised there.

In the case of Model 1, the governing equation of motion is:

$$M\ddot{X}(t) + R(t) = U(t), \tag{21}$$

where the mass M refers to a standard cylindrical cored soil specimen with a cross-sectional area $\frac{\pi D^2}{4}$ and height H. X is the displacement at the top of the specimen, R is the specimen's axial restoring force and

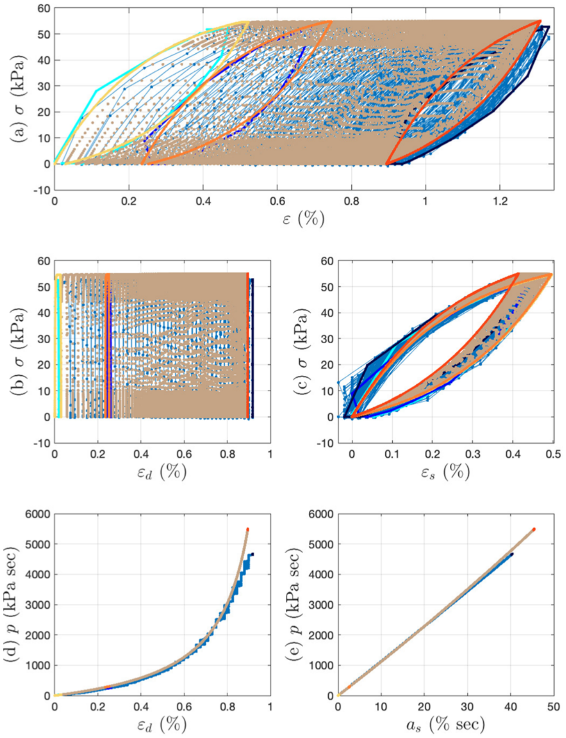

Fig. 26 **a**–**c** Hysteresis loops, and **d** and **e** one-to-one mappings of the first 200 cycles of Test 2 dataset in pale blue, where the first, 11th and 200th cycles are highlighted in cyan, blue, and dark blue, respectively, overlaid with the full-system simulation results in brown, where the first, 11th, and 200th cycles are highlighted in yellow, orange and dark orange, respectively. Model 4 in Table 2 is adopted with $\zeta = 4$. The "event option" under MATLAB ode15s is used with AbsTol $= 10^{-12}$, RelTol $= 10^{-3}$, and Refine $= 1$

U is the applied force due to the trapezoidal loading for Tests 2 and 3 (reproduced in Fig. 2). We have $M = \rho V$ where $V = \frac{\pi D^2}{4} H$ is the volume of a standard soil specimen and its density is $\rho = 2000$ kg/m^3 (given in [28]). Hence $M \approx 1.09$ kg is the mass of a typical soil specimen. Also, we have the applied force, $U(t) = \frac{\pi D^2}{4} u(t)$, at the top of the specimen where $u(t)$ denotes the applied "deviator stress" shown in Fig. 2 of [28].

For a linear dashpot (linear Maxwell model) connected in series with a linear spring, we have:

$$\frac{R}{\tau} + \dot{R} = K\dot{X} \tag{22}$$

where $K = \frac{E_0 \frac{\pi D^2}{4}}{H}$ is the axial stiffness of a cylindrical specimen with Young's modulus equal to E_0 (Hooke's law) and τ is a relaxation time. The estimated value of E_0 for Test 3 is presented in Fig. 13d; similarly E_0 for Test 2 appears in Fig. 23d. Given the modulus for a particular test, the corresponding value of τ was obtained by conducting trial-and-error simulations until the simulated ratcheting strain approximately matched the measured strain data during the first few loading cycles. Table 7 gives the values of E_0 and τ used in these linear dynamic Maxwell simulations.

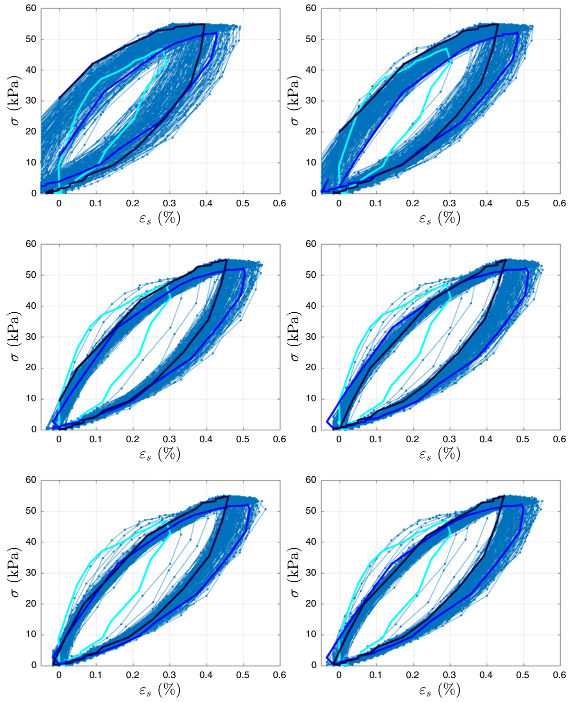

Fig. 27 A parametric study of offset value on the underlying mem-spring's stress–strain plot for Test 3: From left to right, and top to bottom, the offset values are 0, 1, 2, 3, 4, and 5

Simulations were conducted by numerically integrating the coupled ordinary differential equations (ODEs) in Eq. (21) and Eq. (22). After re-writing these ODEs as a system of three first-order ODEs in terms of the three state variables X, $\dot{X}$ and R (as is usually done as reviewed in [39]), we have:

$$\mathbf{Y} = \begin{Bmatrix} Y(1) \\ Y(2) \\ Y(3) \end{Bmatrix} = \begin{Bmatrix} X \\ \dot{X} \\ R \end{Bmatrix}$$

$$\dot{\mathbf{Y}} = \begin{Bmatrix} Y(2) \\ \frac{1}{M}(U(t) - Y(3)) \\ -\frac{Y(3)}{\tau} + KY(2) \end{Bmatrix} \tag{23}$$

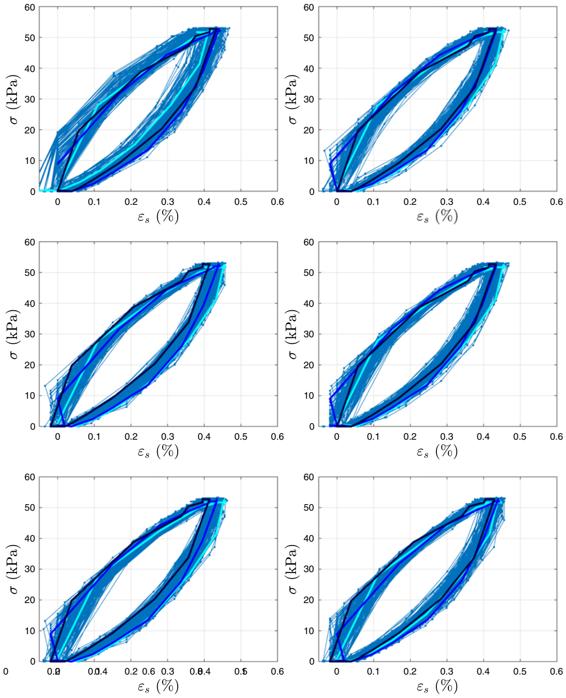

Fig. 28 A parametric study of offset value on the underlying mem-spring's stress–strain plot for Test 2: From left to right, and top to bottom, the offset values are 0, 1, 2, 3, 4, and 5

The simulation results from the first 11 cycles of loading, obtained by numerically integrating Eq. (23), starting with the three initial conditions, $X(0) = 0$, $\dot{X}(0) = 0$ and $R(0) = 0$ are similar to those in Fig. 29. These results illustrate a fundamental flaw of Model 1, namely spurious high-frequency oscillations – corresponding to the natural frequency $\omega_n = \sqrt{K/M}$ – which are absent in the test data. These oscillations are triggered by the piecewise trapezoidal loading $U(t) = \frac{\pi D^2}{4} u(t)$ which has four points in time (per cycle) when the time derivative of the applied force per unit mass changes instantaneously, creating four jerks (units of m/s^3) per cycle. These high-frequency oscillations increase in amplitude with each cycle because the damping introduced by τ is insufficient to remove them. This is especially apparent for larger τ values (e.g., Test 2). As is commonly done, for both physical and numerical reasons, additional damping was introduced to deal with this problem, as described next.

To remove the unwanted and non-physical high-frequency oscillations in Fig. 29, a linear viscous damper was added as shown in Model 2, leading to the following equation of motion:

$$M\ddot{X}(t) + C\dot{X}(t) + R(t) = U(t) \tag{24}$$

where the damping coefficient $C = 2\zeta M\omega_n = 2\zeta\sqrt{MK}$ has been expressed in standard form using the dimensionless parameter ζ (critical damping is $\zeta = 1$). Upon choosing the same three state variables X, $\dot{X}$ and R as above, Eq. (24) and Eq. (22) can be re-written as the following set of three first-order ODEs:

$$\dot{\mathbf{Y}} = \begin{Bmatrix} Y(2) \\ \frac{1}{M}(U(t) - CY(2) - Y(3)) \\ -\frac{Y(3)}{\tau} + KY(2) \end{Bmatrix} \tag{25}$$

The improved simulation results using $\zeta = 1$ for the first 11 cycles of loading are similar to those in Fig. 30.

E Nonlinear simulations involving mem-models

Table 2 presents the scope of all dynamic simulations in this study, and choices of state variables following bond graph theory. Model 1 involves serial connectivity only, while the last three models share mixed connectivity as reasoned in Appendix D. Generalized momentum P and displacement X are selected first and foremost as state variables following the insights in the bond graph theory, as explained in [39]. This series of simulations form a careful validation of the proposed mem-models by progressively making contrast with simpler linear dynamic models to reveal the usefulness of mem-modeling concepts and techniques. Note that Tests 2 and 3 have ratcheting strains (i.e., accumulation of strain) that differ by an order of magnitude; all models in Table 2 are validated using both Tests 2 and 3 data.

Throughout Table 2, mass M and excitation force U follow Appendix D. In addition to the conversions made in Eqs. (1) and (2), we have $P = \frac{\pi D^2}{4} p$.

Modular codes are prepared using MATLAB ode45 or ode15s [48] to facilitate model comparison and justify the usefulness of mem-models.

E1 Overview, choices of state variables, and revisiting linear models

The current subsection reviews the choices for two state variables in bond graph theory, and applies these state variables to Models 1 and 2 in Table 2, which are a Maxwell model and standard fluid model, respectively.

Options to formulate Model 1 are as many as four as discussed in [39]. Given the choice of state variables specified in Table 2, we have:

$$\mathbf{Y} = \begin{Bmatrix} P(t) \\ X(t) \end{Bmatrix}, \tag{26}$$

$$\dot{\mathbf{Y}} = \begin{Bmatrix} R(t) \\ \dot{X}(t) \end{Bmatrix} = \begin{Bmatrix} -\frac{P(t)}{\tau} + KX(t) \\ -\frac{P(t)}{M} + \frac{\int_0^t U(s)ds}{M} \end{Bmatrix} \tag{27}$$

where a typo for this formulation in Table 1 of [39] is corrected. The value for τ follows Appendix D.

For Models 2 and 3 in Table 2, we integrate Eq. (24) with respect to time on both sides, leading to an equivalent equation of motion in an integral form as follows:

$$M\dot{X}(t) + CX(t) + P(t) = \int_0^t U(s)ds \tag{28}$$

from which $\dot{X}(t)$ will be expressed using state variables $P(t)$ and $X(t)$ and excitation $U(t)$, leading to one state equation for both Models 2 and 3.

For the standard fluid model under Model 2, the other state equation is as follows:

$$R(t) = -\frac{P(t)}{\tau} + KX(t) \tag{29}$$

based on deformation compatibility $\varepsilon = \varepsilon_d^L + \varepsilon_s^L$ with the superscript L stands for linear (dashpot and spring). For Model 2, the linear viscous damping is $\zeta = 1$ as in Appendix D. For Models 1 to 3, the linear spring stiffness $K = \frac{E_0 \frac{\pi D^2}{4}}{H}$ follows Appendix D.

Simulation results for Models 1 and 2, which are linear, are presented in Figs. 29 and 30 for the first 11 cycles. The spurious oscillations in Fig. 29 no longer appear in Fig. 30 justifying the need of replacing Model 1 with 2. For Model 2, the comparison with test data steadily worsens if the number of cycles is increased from 11 to 200, as can be seen in Fig. 31a. This was expected since these cyclic triaxial tests were designed to repeatedly stress each specimen beyond its elastic limit. For the ratcheting strain, the concept of the one-to-one mapping between p and ε_d as applied in Fig. 32a vividly indicates the inadequacy of the adopted linear viscous damper. For every cycle, the loading and unloading are the same straight line in terms of σ versus ε_s (not shown). To improve this basic linear elastic dynamic uniaxial model, we explored mem-modeling concepts. It should be noted that more numerical damping, meaning $\zeta = 4$ (or sometimes even more), will be needed when conducting nonlinear simulations using minor loops of the extended Masing model, Sect. 3.2.

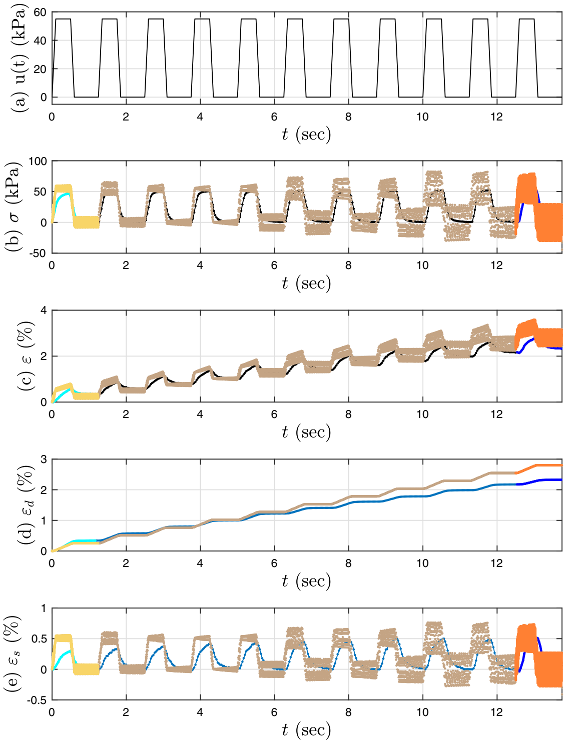

Fig. 29 Time histories of the first 11 cycles of the linear dynamic Maxwell model compared to the Test 3 dataset in black and pale blue, where the first and 11th cycles are highlighted in cyan and blue, respectively, overlaid with the simulation results in brown, where the first and 11th cycles are highlighted in yellow and orange, respectively. Model 1 in Table 2 is adopted with $\tau = 1$. The MATLAB ode45 is used with AbsTol $= 10^{-6}$, RelTol $= 10^{-3}$, and Refine $= 1$

E2 Simulations with mem-dashpot models

For Model 3 where a mem-dashpot replaces the linear dashpot, the other state equation is as follows:

$$R(t) = -\varepsilon_0 K l \frac{\frac{P(t)}{p_0}}{\frac{\pi D^2}{4} + \frac{P(t)}{p_0}} + KX(t) \tag{30}$$

also based on deformation compatibility $\varepsilon = \varepsilon_d + \varepsilon_s^L$ with the first term on the righthand side following Eq. (16), and linear strain $\varepsilon_s^L = \frac{\sigma}{E_0}$. The conversion between the force-displacement and stress–strain expressions called for a careful attention.

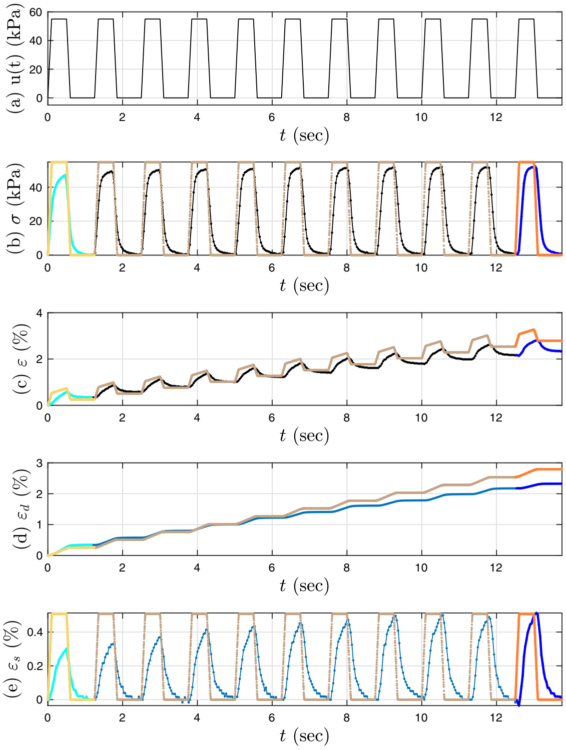

Fig. 30 Time histories of the first 11 cycles of the critically damped linear dynamic Maxwell model compared to the Test 3 dataset in black and pale blue, where the first and 11th cycles are highlighted in cyan and blue, respectively, overlaid with critically damped simulation results in brown, where the first and 11th cycles are highlighted in yellow and orange, respectively. Model 2 in Table 2 is adopted with $\tau = 1$ and $\zeta = 1$. The MATLAB ode45 is used with AbsTol $= 10^{-6}$, RelTol $= 10^{-3}$, and Refine $= 1$

A representative view of the dynamic simulation result using Model 3 is given in Fig. 31b, where it can be seen that the strain ratcheting behavior has been satisfactorily captured for 200 cycles as a whole. Meanwhile, the comparison of the corresponding experimental and simulated one-to-one mapping between p and ε_d in Fig. 32b is consistent. Figures 31 and 32 are designed not only to show the improvement from Models 2 to 3 in terms of modeling ratcheting strain, but also illustrate the conciseness of using the mem-dashpot concept to encode strain ratcheting.

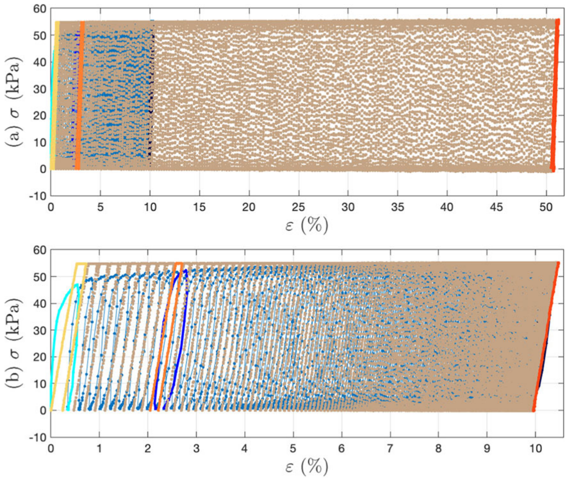

Fig. 31 Hysteresis loops of the first 200 cycles of Test 3 dataset in pale blue, where the first, 11th and 200th cycles are highlighted in cyan, blue, and dark blue, respectively, overlaid with the simulation results in brown, where the first, 11th, and 200th cycles are highlighted in yellow, orange and dark orange, respectively. **a** Model 2 in Table 2 is adopted with $\tau = 1$ and $\zeta = 1$, and **b** Model 3 in Table 2 is adopted with $\zeta = 1$. For both models, the MATLAB ode45 is used with AbsTol $= 10^{-6}$, RelTol $= 10^{-3}$, and Refine $= 1$

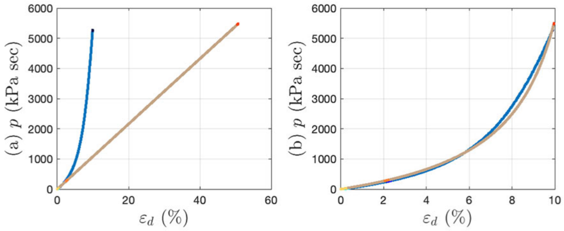

Fig. 32 One-to-one mappings of the first 200 cycles of Test 3 dataset in pale blue, where the first, 11th and 200th cycles are highlighted in cyan, blue, and dark blue, respectively, overlaid with the simulation results in brown, where the first, 11th, and 200th cycles are highlighted in yellow, orange and dark orange, respectively. **a** Model 2 in Table 2 is adopted with $\tau = 1$ and $\zeta = 1$, and **b** Model 3 in Table 2 is adopted with $\zeta = 1$. For both models, the MATLAB ode45 is used with AbsTol $= 10^{-6}$, RelTol $= 10^{-3}$, and Refine $= 1$

The energy dissipated during each cycle, however, is still not captured at all as shown in Fig. 31b. This is because a linear spring is used. Recalling Fig. 14, the energy dissipation from the mem-spring contributes more significantly than the mem-dashpot to the total dissipated energy. Thus, the mem-spring needs to be devised. This motivates Model 4 in Table 2.

E3 Simulation with minor loops of extended Masing model

We benefit from [3] in terms of selecting state variables and determining state equations for the extended Masing model. We have the states and state equations as follows:

$$\mathbf{Y} = \left\{ \begin{array}{c} P(t) \\ R(t) \\ X_M(t) \\ \dot{X}_M(t) \end{array} \right\}, \tag{31}$$

$$\dot{\mathbf{Y}} = \left\{ \begin{array}{c} R(t) \\ \dot{R}(t) \\ \dot{X}_M(t) \\ \ddot{X}_M(t) \end{array} \right\} = \left\{ \begin{array}{c} Y(2) \\ \dot{R}(t) \\ Y(4) \\ \ddot{X}_M(t) \end{array} \right\}$$
$$= \left\{ \begin{array}{l} Y(2) \\ \begin{cases} K^*\left(1 - \frac{Y(2)-0}{2R_u^*}\right) Y(4), & \text{reloading} \\ K^*\left(1 - \frac{R^*-Y(2)}{2R_u^*}\right) Y(4), & \text{unloading} \end{cases} \\ Y(4) \\ \ddot{X}_M(t) \end{array} \right\} \tag{32}$$

where we have applied Eqs. (17) and (18) to $\dot{Y}(2)$ for loading/reloading, and unloading branches, respectively. $K^* = \frac{E\frac{\pi D^2}{4}}{H}$, where $E = \overline{E}\frac{\max(\sigma)}{\max(\varepsilon_s)}$. and $\overline{E}$ follows Eq. (20), while $R_u^* = \sigma_u \frac{\pi d^2}{4}$, where $\sigma_u = \overline{\sigma}_u \max(\sigma)$, and $\overline{\sigma}$ follows Eq. (19). R^* is the restoring force at the pivoting value where $\dot{X}_M = 0$ and $\dot{R} = 0$ simultaneously. These three variables, each marked with an asterisk, are algebraic variables in this formulation.

The expression for $Y(4) = \ddot{X}_M(t)$ can be obtained continuing with Eq. (24) as follows:

$$M\left(\ddot{X}_d(t) + \ddot{X}_M(t)\right) + C\left(\dot{X}_d(t) + \dot{X}_M(t)\right) + R(t) = U(t) \tag{33}$$

$$\left(\ddot{X}_d(t) + \ddot{X}_M(t)\right) + \frac{C}{M}\left(\dot{X}_d(t) + \dot{X}_M(t)\right) + \frac{R(t)}{M} = \frac{U(t)}{M} \tag{34}$$

Knowing that $X_d(t) = F_d(P(t))$, we have $\dot{X}_d(t) = \frac{dF_d(P)}{dP}\frac{dP}{dt} = \frac{dF_d(P)}{dP}R$ and $\ddot{X}_d(t) = \frac{d^2F_d(P)}{dP^2}R^2 + \frac{dF_d(P)}{dP}\dot{R}$, and then:

$$\ddot{X}_M(t) = -\frac{R(t)}{M} - \frac{C}{M}\left(\dot{X}_d(t) + \dot{X}_M(t)\right) + \frac{U(t)}{M} - \ddot{X}_d(t) \tag{35}$$

$$\ddot{X}_M(t) = -\frac{R(t)}{M} - \frac{C}{M}\left(\frac{dF_d(P)}{dP}R + \dot{X}_M(t)\right) + \frac{U(t)}{M} - \left(\frac{d^2F_d(P)}{dP^2}R^2 + \frac{dF_d(P)}{dP}\dot{R}\right) \tag{36}$$

directly leads to the important state equation. In summary, Eq. (36) is for $\dot{Y}(4)$. In addition to the four state variables, there are three algebraic variables in this formulation. This formulation is thus a differential algebraic equation (DAE) - not an ODE. See [5].

The use of the "event" option, i.e., the state event location algorithm [47], is critical, while the underlying mathematical background is a hybrid dynamical system as outlined in [3,39,41,57]. There are two modes for this system: loading (including initial loading and reloading) versus unloading. A mode indicator tag_2, following the notation used in our publications, take the values of 1 and -1 associated with loading and unloading mode, respectively. The flow maps for both modes are given in Eq. (32). The event functions are:

$$\text{Event Type\#1}: Y(4) = 0, \text{ when } Y(4) \text{ is ascending} \tag{37}$$

$$\text{Event Type\#2}: Y(4) = 0, \text{ when } Y(4) \text{ is descending} \tag{38}$$

The reset map contains assigning $Y(4) = 0$ and $tag_2 = -tag_2$ on all occasions. Additionally, at an Event Type #1, both K^* and R_u^* values will be updated. These two values will be held constant within the cycle. At an Event Type #2, assign the current value of $Y(2)$ to R^*. This R^* value will be held constant for the rest of the cycle.

Using the first 11 cycles for a more effective visualization, Figs. 33 and 19 present the time histories, and hysteresis loops and one-to-one mappings, respectively. In these two figures, the first and 11th cycles are highlighted for this time-varying system. Figure 34 repeats Fig. 33 but highlighting the two types of events defined in Eqs. (37) and (38). It can be seen that Event Types #1 and #2 are correctly captured for each cycle. This is achieved by properly choosing the MATLAB values of relative and absolute tolerances (shorthanded as RelTol and AbsTol, respectively) following [48]. In addition to the state variables, which vary continuously with time, Fig. 35 presents how modes switch from loading to unloading within each cycle, and how the three algebraic variables evolve from cycle to cycle.

Eventually, Fig. 18 serves as a snapshot for the simulated first 200 cycles, where the first, 11th, and 200th cycles are highlighted to emphasize their differences,

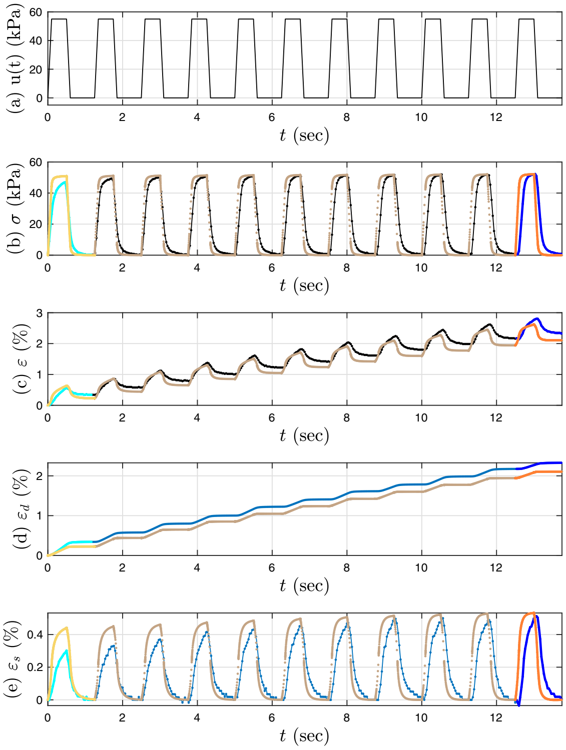

Fig. 33 Time histories of the stress and strains of the first 11 cycles of Test 3 dataset in black and pale blue, where the first and 11th cycles are highlighted in cyan and blue, respectively, overlaid with the simulation results in brown, where the first and 11th cycles are highlighted in yellow and orange, respectively. Model 4 in Table 2 is adopted with $\zeta = 4$. The "event option" under MATLAB ode15s is used with AbsTol $= 10^{-12}$, RelTol $= 10^{-3}$, and Refine $= 1$

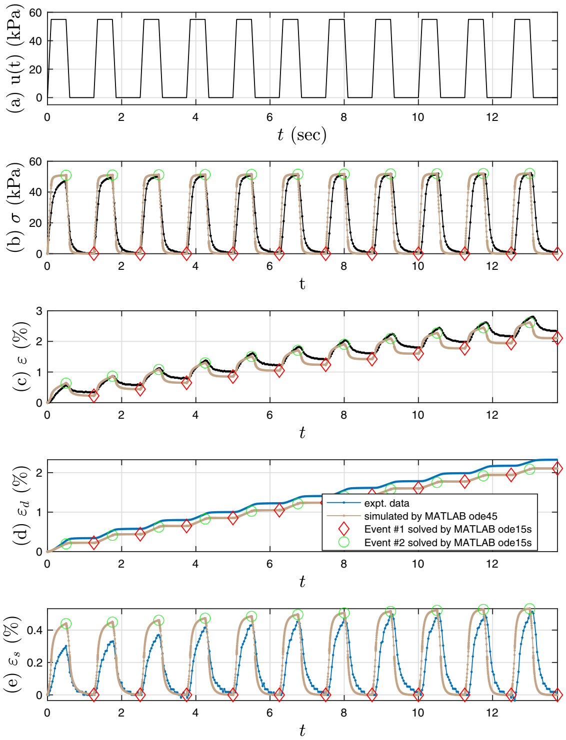

Fig. 34 Time histories of the stress and strains of the first 11 cycles of Test 3 dataset in black and pale blue, overlaid with the full-system simulation results in brown. Model 4 in Table 2 is adopted with $\zeta = 4$. The "event option" under MATLAB ode15s is used with AbsTol $= 10^{-12}$, RelTol $= 10^{-3}$, and Refine $= 1$. The first and second types of events are marked in red diamonds and green circles, respectively

in comparison with the decomposed experimental data. Figure 36 further investigates the dissipated energy from cycle to cycle, which is another effective means to assess the performance of the proposed Model 4.

Given the stiff nature of Model 4 and the need to damp out a range of of higher frequencies associated with the minor loops of the Masing model in our simple uniaxial model, results using increasing ζ values are presented in Fig. 37. It can be seen that there may not be an ideal choice for this value.

As an adaptive time stepping scheme, ode15s in MATLAB does not have fixed time steps. The control of time step is done through specifying AbsTol, RelTol, MaxStep, and InitialStep via odeset. Following [57], the accuracy of our numerical solutions is assessed by studying the global error (GE) of the displacement at a specific time t_n:

$$\mathrm{GE}(t_n) = |\hat{X}(t_n) - X(t_n)| \tag{39}$$

where $X(t_n)$ is the exact displacement at t_n, and $\hat{X}(t_n)$ is the approximated displacement at that time. Since the exact displacement is unknown, we obtain a converged solution by using a very small value of RelTol in MATLAB. In each numerical solution in this study, we fix the value of AbsTol, thus allowing the value of RelTol to control the approximation accuracy. This is the so-called tolerance proportionality (TP) property (see [7] for a review). The work-accuracy diagram [49,50], as the name implies, quantifies the work (measured by either the elapsed time or number of function evaluation (FE)) versus accuracy (measured by GE). The tolerance proportionality (TP) diagram and work-accuracy diagrams are presented in Fig. 38. Both TP and work-accuracy diagrams indicate good computational stability for the numerical solution, meaning that a small

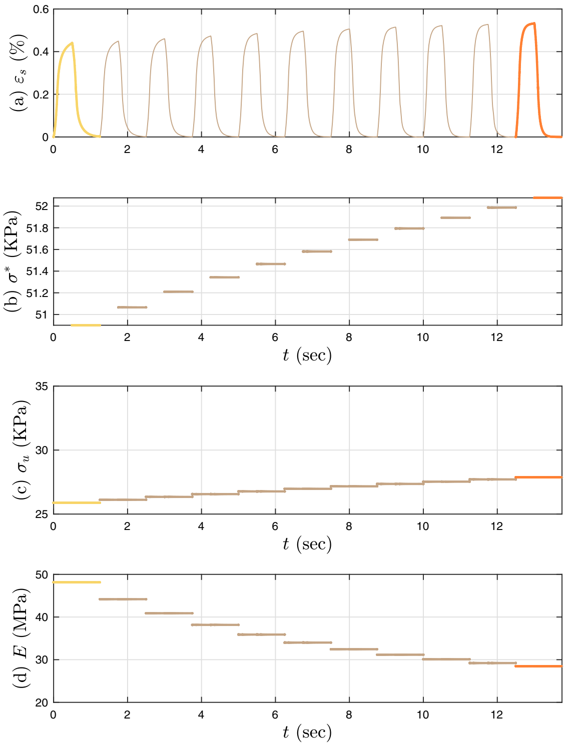

Fig. 35 Time histories of the modes and three algebraic variables of the first 11 cycles of Test 3 of the simulation results in brown, where the first and 11th cycles are highlighted in yellow and orange, respectively. Model 4 in Table 2 is adopted with $\zeta = 4$. The "event option" under MATLAB ode15s is used with AbsTol $= 10^{-12}$, RelTol $= 10^{-3}$, and Refine $= 1$

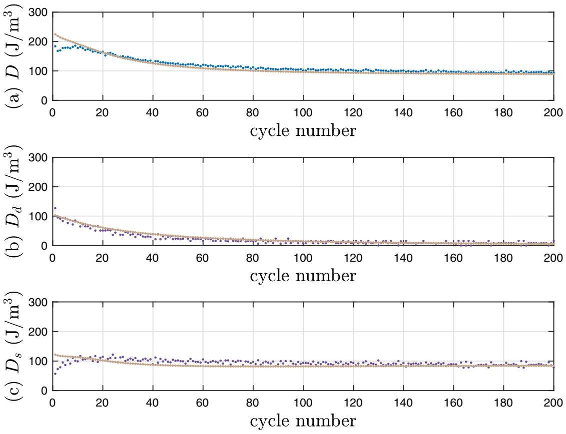

Fig. 36 Dissipated energy for the first 200 cycles of Test 3 obtained using the raw and decomposed experimental data in pale blue and purple, respectively, overlaid with the full-system simulation results in brown. Model 4 in Table 2 is adopted with $\zeta = 4$. The "event option" under MATLAB ode15s is used when with AbsTol $= 10^{-12}$, RelTol $= 10^{-3}$, and Refine $= 1$

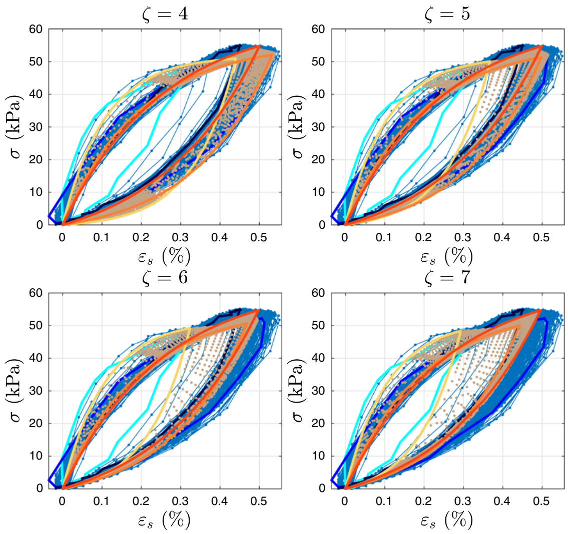

Fig. 37 Hysteresis loops of the first 200 cycles of Test 3 dataset in pale blue, where the first, 11th and 200th cycles are highlighted in cyan, blue, and dark blue, respectively, overlaid with the full-system simulation results in brown, where the first, 11th, and 200th cycles are highlighted in yellow, orange and dark orange, respectively. Model 4 in Table 2 is adopted with $\zeta = 4$, 5, 6, and 7. The "event option" under MATLAB ode15s is used with AbsTol $= 10^{-12}$, RelTol $= 10^{-3}$, and Refine $= 1$

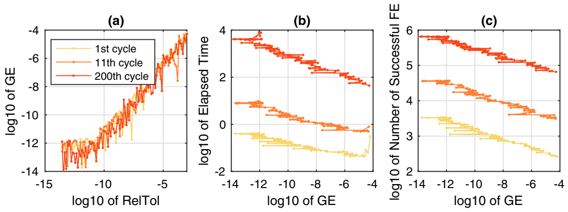

Fig. 38 **a** TP, and **b** and **c** work-accuracy diagrams for X, the third state variable, at the end of the first, 11th, and 200th cycles of Test 3 obtained using the full-system simulation results. Model 4 in Table 2 is adopted with $\zeta = 4$. The "event option" under MATLAB ode15s is used when AbsTol $= 10^{-12}$, and Refine $= 1$. GE stands for global error, while FE stands for function evaluation

change in RelTol leads to a small change in GE, accompanied by a small change in both elapsed time and number of function evaluation.

It is worthwhile to highlight the numerical tools in this study, as a continuation of our applications of Professor Larry Shampine's ODE solvers under MATLAB [48] to hysteresis modeling [3,39,45,57,58]. We appreciate the efficiency and convenience of using ode45 versus RK4, and the power of ode15s to solve stiff ODEs. Both ode45 and ode15s have the option of "event" to implement the state event location algorithm.

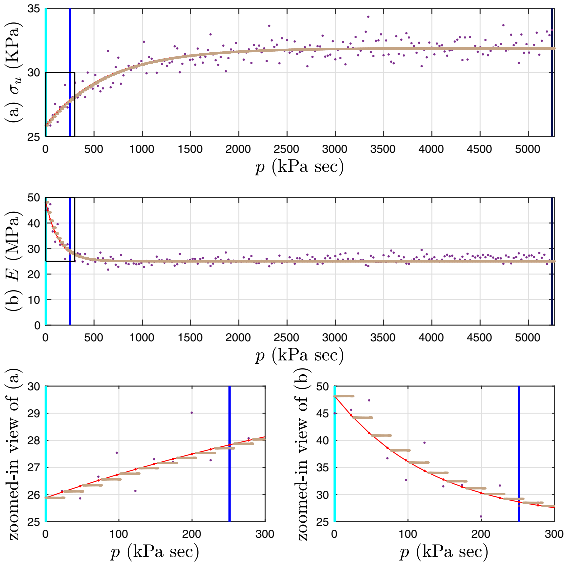

Fig. 39 Verification of the σ_u and E values used for the simulation of the first 200 cycles of Test 3 in contrast with Fig. 17. Model 4 in Table 2 is adopted with $\zeta = 4$. The "event option" under MATLAB ode15s is used when with AbsTol $= 10^{-12}$, RelTol $= 10^{-3}$, and Refine $= 1$

Model 4 in Table 2 is solved using ode15s with "event". Theoretically, DAE and hybrid dynamical system theory will further guide us. For DAE, Fig. 39 first serves an example to illustrate the behavior of algebraic variables in this study. Figure 35c and d should be recalled for Fig. 39a and b, respectively. The values for these two algebraic variables are held constant within each cycle, which demonstrates how to use the two fitted functions in Fig. 17. Global variables are used in the simulation of Model 4, despite the discouragements from mathworks.com. Figure 39 also verifies our uses of global variables, in addition to the TP diagram given in Fig. 38.

References

1. Baber, T.T., Noori, M.N.: Random vibration of degrading, pinching systems. ASCE J. Eng. Mech. **111**(8), 1010–1026 (1985)
2. Beck, J.L., Jayakumar, P.: Class of masing models for plastic hysteresis in structures. In: Proceedings 14th ASCE Structures Congress, Chicago, IL (1996)
3. Beck, J.L., Pei, J.S.: Demonstrating the power of extended masing models for hysteresis through model equivalencies and numerical investigation. Nonlinear Dyn. **108**(2), 827–856 (2022)
4. Bouc, R.: Modèle mathématique d'hystérésis. Acustica **21**, 16–25 (1971)
5. Brenan, K.E., Campbell, S.L., Petzold, L.R.: Numerical Solution of Initial-Value Problems in Differential-Algebraic Equations, 2nd edn. Society for Industrial and Applied Mathematics (1987)
6. Brokate, M., Sprekels, J.: Hysteresis and Phase Transitions, Applied Mathematical Sciences, vol. 121. Springer (1996)
7. Calvo, M., González-Pinto, S., Montijano, J.I.: Global error estimation based on the tolerance proportionality for some adaptive Runge-Kutta codes. J. Comput. Appl. Math. **218**(2), 329–341 (2008)
8. Canfield, R.: central_diff.m. (2015) http://www.mathworks.com/matlabcentral/fileexchange/12-central-diff-m/content/central_diff.m
9. Caughey, T.K.: Random excitation of a system with bilinear hysteresis. J. Appl. Mech. **27**, 649–652 (1960)
10. Caughey, T.K.: Sinusoidal excitation of a system with bilinear hysteresis. J. Appl. Mech. **27**, 640–643 (1960)
11. Chiang, D.Y.: The generalized masing models for deteriorating hysteresis and cyclic plasticity. Appl. Math. Model. **23**, 847–863 (1999)
12. Chua, L.O.: Memrister - the missing circuit element. IEEE Trans. Circuit Theory CT **18**(5), 507–519 (1971)
13. Chua, L.O., Kang, S.M.: Memristive devices and systems. Proc. IEEE **64**, 209–223 (1976)
14. Di Ventra, M., Pershin, Y.V., Chua, L.O.: Circuit elements with memory: Memristors, memcapacitors, and meminductors. Proceedings of IEEE **97**, 1717–1724 (2009)
15. Iwan, W.D.: A distributed-element model for hysteresis and its steady-state dynamic response. ASME J. Appl. Mech. **33**(4), 893–900 (1966)
16. Iwan, W.D.: On a class of models for the yielding behavior of continuous and composite systems. ASME J Appl Mech **34**(3), 612–617 (1967)
17. Jayakumar, P.: Modeling and identification in structural dynamics. PhD thesis, California Institute of Technology, Pasadena, CA (1987)
18. Jayakumar, P., Beck, J.L.: System identification using nonlinear structural models. In: Nake HG, Yao JTP (eds) Structural Safety Evaluation Based on System Identification Approaches, Friedr. Vieweg & Sohn Braunschweig/Wiesbaden, Vieweg International Scientific Book Series, vol Proceedings of the Workshop at Lambrecht/Pfalz, pp 82–102 (1988)
19. Jeltsema, D.: Memory elements: A paradigm shift in lagrangian modeling of electrical circuits. In: Proc. MathMod Conference, Vienna (2012)
20. Jennings, P.C.: Periodic response of a general yielding structure. J. Eng. Mech. Div. Proc. Am. Soc. Civ. Eng. **90**(EM2), 131–166 (1964)
21. Karnopp, D.C., Margolis, D.L., Rosenberg, R.C.: System Dynamics: Modeling, Simulation, and Control of Mechatronic Systems, 5th edn. John Wiley & Sons Inc (2012)
22. Kerschen, G., Worden, K., Vakakis, A.F., Golinval, J.C.: Past, present and future of nonlinear system identification in structural dynamics. Mech. Syst. Signal Process. **20**(3), 505–592 (2006)
23. Krasnosel'skiĭ, M.A., Pokrovskiĭ, A.V.: Systems with Hysteresis. Springer (1983)
24. Lakes, R.S.: Viscoelastic Solids. CRC Press (1998)

25. Mann, S., Janzen, R., Post, M.: Hydraulophone design considerations: absement, displacement, and velocity-sensitive music keyboard in which each key is a water jet. In: Proceedings of the 14th ACM International Conference on Multimedia, Santa Barbara, CA, pp 519–528 (2006)
26. Masing, G.: Eigenspannungen und verfestigung beim messing. In: Proceedings of the 2nd International Congress for Applied Mechanics, Zurich, Switzerland, pp 332–335, in German (1926)
27. Mayergoyz, I.: Mathematical Models of Hysteresis and Their Applications. Elsevier Series in Electromagnetism, Elsevier (2003)
28. Miller, G., Teh, S., Li, D., Zaman, M.: Cyclic shear strength of soft railroad subgrade. ASCE J. Geotech. Geoenviron. Eng. **126**(2), 139–147 (2000)
29. Mitsoulis: 50 years of K-BKZ constitutive relation for polymers. ISRN Polymer Science (Article ID 952379):22 (2013)
30. Morris, K.A.: What is hysteresis? Applied Mechanics Review 64(5):14 pages (2011)
31. Noël, J.P., Kerschen, G.: Nonlinear system identification in structural dynamics: 10 more years of progress. Mech. Syst. Signal Process. **83**, 2–35 (2017)
32. Oh, J., Drincic, B., Bernstein, D.S.: Nonlinear feedback models of hysteresis. IEEE Control Syst. Mag. **29**(1), 100–119 (2009)
33. Oster, G.F., Auslander, D.M.: The memristor: A new bond graph element. ASME J. Dyn. Syst. Measure. Control **94**(3), 249–252 (1973)
34. Paynter, H.M.: Analysis and Design of Engineering Systems: Class Notes for M.I.T. Course 2.751. M.I.T. Press (1961)
35. Paynter, H.M.: The gestation and birth of bond graphs. (2000) http://www.me.utexas.edu/~longoria/paynter/hmp/Bondgraphs.html
36. Pei, J.S.: Mem-spring models combined with hybrid dynamical system approach to represent material behavior. ASCE Journal of Engineering Mechanics (2018)
37. Pei, J.S., Wright, J.P., Todd, M.D., Masri, S.F., Gay-Balmaz, F.: Understanding memristors and memcapacitors for engineering mechanical applications. Nonlinear Dyn. **80**(1), 457–489 (2015)
38. Pei, J.S., Gay-Balmaz, F., Wright, J.P., Todd, M.D., Masri, S.F.: Dual input-output pairs for modeling hysteresis inspired by mem-models. Nonlinear Dyn. **88**(4), 2435–2455 (2017)
39. Pei, J.S., Wright, J.P., Gay-Balmaz, F., Beck, J.L., Todd, M.D.: On choosing state variables for piecewise-smooth dynamical system simulations. Nonlinear Dynamics (2018)
40. Pei, J.S., Carboni, B., Lacarbonara, W.: Mem-models as building blocks for simulation and identification of hysteretic systems. Nonlinear Dynamics (2020a)
41. Pei, J.S., Quadrelli, M.B., Wright, J.P.: Mem-models and state event location algorithm for a prototypical aerospace system. Nonlinear Dynamics (2020b)
42. Pei, J.S., Gay-Balmaz, F., Luscher, D.J., Beck, J.L., Todd, M.D., Wright, J.P., Qiao, Y., Quadrelli, M.B., Farrar, C.R., Lieven, N.A.J.: Connecting mem-models with classical theories. Nonlinear Dynamics (2021)
43. Preisach, F.: About the magnetic aftereffect. Mag. Phys. **94**(5–6), 277–302 (1935)
44. Rosenberg, R.C., Karnopp, D.C.: Introduction to Physical System Dynamics. McGraw-Hill Series in Mechanical Engineering, McGraw-Hill, Inc (1983)
45. Sarles, S.A., Wright, J.P., Pei, J.S.: Equilibrium analysis of mott memristor reveals criterion for negative differential resistance. Appl. Phys. Lett. **118**(22), 223505 (2021)
46. Schoukens, M., Tóth, R.: Linear parameter varying representation of a class of mimo nonlinear systems. IFAC-PapersOnLine **51**(26), 94–99 (2018)
47. Shampine, L.F., Gladwell, I., Brankin, R.W.: Reliable solution of special event location problems for odes. ACM Trans. Math. Softw. **17**(1), 11–25 (1991)
48. Shampine, L.F., Gladwell, I., Thompson, S.: Solving ODEs with MATLAB. Cambridge University Press, New York (2003)
49. Söderlind, G.: Automatic control and adaptive time-stepping. Numer. Algorithms **31**(1–4), 281–310 (2002)
50. Söderlind, G., Wang, L.: Adaptive time-stepping and computational stability. J. Comput. Methods Sci. Eng. **2**(3), 1–19 (2003)
51. Strukov, D.B., Snider, G.S., Stewart, D.R., Williams, R.S.: The missing memristor found. Nature **453**, 80–83 (2008)
52. Swevers, J., Al-Bender, F., Ganseman, C.G., Prajogo, T.: An integrated friction model structure with improved presliding behavior for accurate friction compensation. IEEE Trans. Autom. Control **45**(4), 675–686 (2000)
53. Visintin, A.: Differential Models of Hysteresis. Springer (1994)
54. Wagg, J.D., Pei, J.S.: Modeling helical fluid inerter system with invariant mem-models. Journal of Structural Control and Health Monitoring (2020)
55. Wang, T., Noori, M., Altabey, W.A., Wu, Z., Ghiasi, R., Kuok, S.C., Silik, A., Farhan, N.S., Sarhosis, V., Farsangi, E.N.: From model-driven to data-driven: A review of hysteresis modeling in structural and mechanical systems. Mech. Syst. Signal Process. **204**(110), 785 (2023)
56. Wen, Y.K.: Method for random vibration of hysteretic systems. ASCE J. Eng. Mech. **102**(2), 249–263 (1976)
57. Wright, J.P., Pei, J.S.: Solving dynamical systems involving piecewise restoring force using state event location. ASCE J. Eng. Mech. **138**(8), 997–1020 (2012)
58. Wright, J.P., Sarles, S.A., Pei, J.S.: DC operating points of mott neuristor circuits. Microeletr. Eng. **284–285**, 112124 (2024)